Hindawi Publishing Corporation
Advances in Optical Technologies
Volume 2008, Article ID 279502, 32 pages
doi:10.1155/2008/279502

Review Article

Silicon Nanocrystals: Fundamental Theory and Implications for Stimulated Emission

V. A. Belyakov,[1] V. A. Burdov,[1] R. Lockwood,[2] and A. Meldrum[2]

[1] *Department of Theoretical Physics, University of Nizhniy Novgorod, pr. Gagarina 23, Nizhniy Novgorod 603950, Russia*
[2] *Department of Physics, University of Alberta, Edmonton, AB, Canada T6G2G7*

Correspondence should be addressed to A. Meldrum, ameldrum@ualberta.ca

Received 18 February 2008; Accepted 9 May 2008

Recommended by D. Lockwood

Silicon nanocrystals (NCs) represent one of the most promising material systems for light emission applications in microphotonics. In recent years, several groups have reported on the observation of optical gain or stimulated emission in silicon NCs or in porous silicon (PSi). These results suggest that silicon-NC-based waveguide amplifiers or silicon lasers are achievable. However, in order to obtain clear and reproducible evidence of stimulated emission, it is necessary to understand the physical mechanisms at work in the light emission process. In this paper, we report on the detailed theoretical aspects of the energy levels and recombination rates in doped and undoped Si NCs, and we discuss the effects of energy transfer mechanisms. The theoretical calculations are extended toward computational simulations of ensembles of interacting nanocrystals. We will show that inhomogeneous broadening and energy transfer remain significant problems that must be overcome in order to improve the gain profile and to minimize nonradiative effects. Finally, we suggest means by which these objectives may be achieved.

1. INTRODUCTION

Silicon is the most widespread semiconductor in modern microelectronics technologies. Its natural abundance, low cost, and high purity, as well as the high electronic quality of the Si/SiO_2 interface, have led to its overwhelming dominance in microelectronic devices. Nevertheless, the use of silicon in optoelectronics remains highly limited. This state of affairs has remained, in fact, almost unchanged because of a fundamental property of the silicon band structure—the indirect band gap.

The indirect radiative interband transitions in bulk Si are strongly suppressed because an emitted photon cannot satisfy the momentum conservation law for transitions from the conduction-band minimum (Δ-point) to the top of the valence band (Γ-point). The photon wave vector is about three orders of magnitude less than that required for the transition between the Δ- and Γ-points. This difference in $\mathbf{k}$-space is $k_\Delta = 0.86 \times 2\pi/a_0$, with a_0 being the lattice constant of silicon, equal to 5.43 Å. The electron-hole radiative recombination in the bulk material is exactly forbidden unless additional mechanisms allowing the momentum to be conserved are involved in the recombination process. The most probable means to have a radiative indirect transition without breakdown of the momentum conservation law is via phonon absorption or emission. However the electron-phonon interaction is weak; consequently, phonon assistance is a low-probability (and hence slow) process. This leads to a substantial increase of the total recombination time, and a decrease of the recombination probability compared to the direct no-phonon $\Gamma - \Gamma$ radiative transitions in direct-gap semiconductors. In this sense, we call such transitions in Si "strongly suppressed."

The discovery of visible-range emission from nanocrystalline [1] and porous [2–4] silicon in the early 1990s suggested that some of the problems associated with the silicon band structure might be overcome in nanoscale crystallites hosted in a widegap dielectric matrix like SiO_2, in order to create a strong confining potential for carriers inside the nanocrystal. Electronic states become localized within the NC and the momentum distribution spreads due to the Heisenberg uncertainty relations. In other words, the wave functions consist of plane waves with all possible wave vectors including both $k \sim k_\Delta$ for holes and $k \sim 0$ for electrons,

respectively. Thus, the momentum conservation law is not violated in this case, which yields a nonzero probability of the $\Delta - \Gamma$ radiative transition even in the absence of phonons.

Indeed, some time later, efficient visible photoluminescence (PL) from silicon nanocrystals was experimentally demonstrated, (e.g., [5]) and attributed to the transitions between confined electron and hole states inside the nanocrystal [6, 7] (the so-called quantum confinement effect) or between interface states [8, 9]. However, the emission quantum efficiency in Si nanocrystals remains low compared to the direct gap III-V or II-VI materials. This is naturally explained by the small "weights" of the plane waves with $k \sim k_\Delta$ for the valence states and $k \sim 0$ for the conduction states. Thus, improvement of the light emission efficiency of Si quantum dots remains a challenge for optoelectronic technologies.

As a means to modify the optical properties of silicon crystallites, doping with shallow impurities has been suggested [10–18]. In some cases (depending on the conditions and methods of preparation), the emitting properties of the dots were improved significantly. In particular, the PL intensity was several times greater when the nanocrystals were doped with phosphorus [10–12, 14] or codoped with phosphorus and boron [15, 17]. The origin of this phenomenon is not fully understood at the present time, and we will touch on the problem of impurity states in silicon nanocrystals in this review.

PL experiments are not usually carried out with a single quantum dot but rather with large ensembles. As a result, interpretation of the experimental data is attendant with difficulties because of the associated inhomogeneous broadening and various collective effects that can occur as a result of the mutual influence of the nanocrystals in the ensemble. Some recent studies have reported on the PL spectra of individual silicon quantum dots [19, 20] and this is shedding new light on the physics involved in the light emission process. A principal distinction in the emission of a single NC and a nanocrystal ensemble lies in the various mechanisms of interaction amongst the nanocrystals in an ensemble. In particular, in solid nanocrystal arrays, some collective effects caused by electron, photon, and phonon transfer between the dots can strongly influence the luminescence dynamics of the nanocrystals in comparison with the case of isolated NCs. The size distribution of the nanocrystals can play an essential role in the excitation exchange between the clusters.

One possible mechanism of the NC-NC interaction is the direct tunneling of excited carriers from one quantum dot to another [21–23]. As an example, we can imagine two (or more) closely separated quantum dots with different sizes. Presumably, excited carriers in the smaller nanocrystal, having higher quantized energy levels, may relax either to the valence band of this nanocrystal or to the conduction band of the adjacent nanocrystal with a larger size. The transition to the valence band is indirect, and therefore suppressed. Meanwhile, the transfer to the neighboring quantum dot occurs as if within the same (conduction) band, and may be more probable in the case where the nanocrystals are sufficiently close. If so, then the smaller nanocrystals will inject their own excited carriers into the larger nanocrystals, in which radiative interband transition will subsequently take place. This idea implies the possibility of an optical nanofountain [24]—a device emitting photons from the area where quantum dots with larger sizes are concentrated.

An additional nonradiative mechanism of energy transfer between adjacent nanocrystals becomes possible in dense arrays. This is the so-called Forster mechanism originating from the dipole-dipole (or higher-order multipole) interaction between excitons in different quantum dots [25–27]. Because of the dipole-dipole interaction, the electron-hole excitations can "travel" throughout the nanocrystals without charge transfer. Such transitions have been observed in solid arrays of CdSe nanocrystals [28, 29]. Some theoretical aspects of the Forster transfer in silicon quantum dots were recently discussed by Allan and Delerue [30].

Various collective effects in quantum-dot arrays can result in a complicated time dependence of the experimental PL decay. As a rule, the decay is described by the stretched exponential function $\exp\{-(t/\tau)^\beta\}$ with β less than unity [31–35]. Evidently, the value of β can be due to a size distribution of the nanocrystals (and hence a distribution of the recombination rates). Theoretical explanations of the stretched exponential from the point of view of the multiexponential decay and associated Laplace transforms have been given in [36].

This is, in short, the framework in which we will address the present review. At first we will briefly describe the experimental situation in this field in Section 2. Then the single-particle electronic structure and many-body corrections will be considered in Section 3 for a single silicon quantum dot as a basis for treatment of more complicated problem of solid quantum-dot ensembles. The latter will be reviewed in Section 4. Finally, Section 5 presents a general conclusion and a commentary on the potential for stimulated emission in silicon nanocrystal ensembles.

2. EXPERIMENTAL RESULTS: OVERVIEW

Different methods can be used for preparation of silicon nanocrystals, for instance, Si ion implantation [37–41], chemical vapor deposition [42], magnetron sputtering [43, 44], colloidal synthesis [45], electron beam evaporation [46, 47], and some others. A high-temperature thermal treatment is generally required in order to precipitate the crystallites. All these techniques allow one to form silicon NCs with sizes predominantly ranging from 2–6 nm. Their electronic structure and optical properties depend, of course, on the preparation conditions and method of fabrication. However, there are some common properties typical for silicon NCs, independent of the fabrication technique employed. In particular, the nanocrystals' surroundings, either vacuum or some host material like silicon dioxide, represent a high potential barrier for carriers of both kinds. Such a barrier is often referred to as a confining potential that mainly defines the energy spectrum of the nanocrystal. In what follows we will discuss some manifestations of the quantum-confinement effect in experiments and theoretical models.

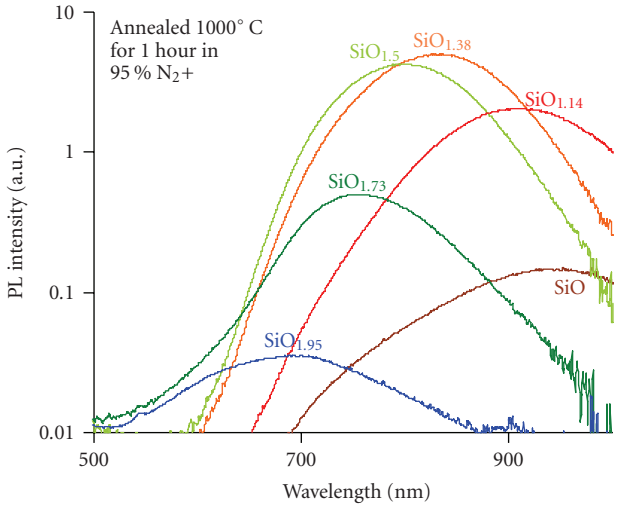

FIGURE 1: PL spectra of silicon NCs in SiO_2. The 200-nm-thick samples were approximately identical except for the amount of excess silicon.

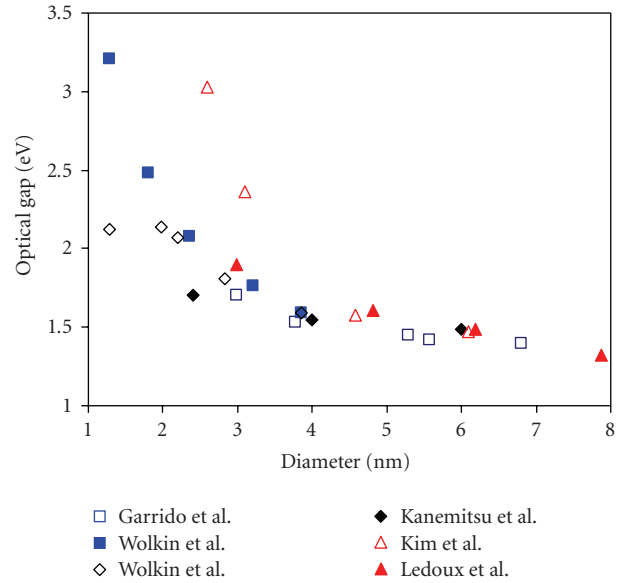

FIGURE 2: Experimental data on the size dependence of the optical gap of silicon crystallites. Hydrogen-passivated surface—Wolkin et al. [8] and Garrido et al. [53] (blue squares); SiO-bonds at the surface—Wolkin et al. [8], Kanemitsu et al. [51] (diamonds); deposition on quartz substrate—Ledoux et al. [48] (filled triangles); nanocrystals embedded in Si_3N_4 matrix—Kim et al. [49] (empty triangles).

First, let us briefly discuss experimental data on the PL spectra in silicon quantum dots.

2.1. Size dependence

As has been mentioned above, silicon NCs are capable of emitting electromagnetic energy in the visible spectrum. This is in contrast with bulk silicon, in which energy of the interband transition corresponds to the silicon bandgap energy of 1.12 eV. The increase (decrease) of the photon frequency (wavelength) in nanocrystals compared to the bulk material is a universal phenomenon taking place in various semiconductor materials and quantum dots. In the general case one may say that the energy of the emitted photon increases as the nanocrystal size decreases. Such an increase is usually called a "blueshift" because the photon energy shifts toward the shorter-wavelength side of the visible spectrum. This blueshift is illustrated for Si NCs in Figure 1. Here, the mean NC size is controlled via the excess Si concentration, with the smallest NCs occurring in the most silicon deficient samples. The PL intensity has not been normalized here; the drop in intensity on the silicon-poor side of the compositional map is due to the lower number density of NCs, and on the silicon-rich side it is due to the opening of nonradiative pathways in large and highly interconnected nanoclusters.

In the simplest model of an infinitely strong confining potential (i.e., infinitely high potential barriers at the dot boundary) it is possible to estimate the energies of electrons and holes localized inside the nanocrystal as proportional to R^{-2}, where R is the nanocrystal radius. Thus, the optical gap may be calculated as $\varepsilon_g(R) = \varepsilon_g + A/R^2$, where ε_g is the bandgap of bulk silicon, A is some positive constant, and A/R^2 represents the total energy of the non-interacting electron-hole pairs inside the dot. It is obvious that: (i) the nanocrystal gap must be always greater than the bulk one due to the additional positive term A/R^2, and (ii) the photon energy, equal to the energy of the lowest electron-hole transition, increases as the dot size decreases.

In experimental work carried out over the past fifteen years with silicon nanocrystals, the optical-gap dependence on the dot size was measured and discussed extensively. Although it is impractical to cite all the papers dealing with this topic, a sampling is given in [8, 23, 48–56]. The data in these papers is summarized in Figure 2. There is a fairly large spread in the calculated values of the optical gaps as a function of NC diameter. Presumably, several factors influencing the accuracy of the optical-gap measurements are as follows. First, it is difficult to determine exactly the dot sizes and the size distribution in a luminescent ensemble of NCs. Second, using the mean size in an ensemble of NCs in a diagram like Figure 2 can be misleading, since it is possible that the observed PL peak does not correspond exactly to the mean size but instead to the largest PL rate. Third and more practically, the nanocrystals studied by different research groups have been prepared by different methods. As a result, the NCs have different surroundings, surface bonds, and shapes, all of which could lead to scatter in the experimental data. Finally, as shown in later sections, NC-NC interactions can play a dominant role in the emission spectrum.

Furthermore, the blue-shift energy $\Delta\varepsilon_g(R)$, determined from the experiments, does not obey the law A/R^2 following from the simplest quantum-mechanical model. This dependence is rather $\Delta\varepsilon_g(R) \sim R^{-b}$ with $1 < b < 1.5$ or an even weaker dependence on R in some cases. Such behavior has been a reason for supposing a key role for interface states in

the radiative recombination process [51]. The question about the origin of the radiative electron-hole transitions in the nanocrystals is remains under extensive debate even today.

Nevertheless, employing the principle of Occam's razor, the deviations from the simplest model predictions for high-energy luminescence (when the peak-position energy exceeds the bulk gap ε_g) may be explained within the quantum confinement framework without necessarily the need to invoke sub-gap radiative centers. Let us, first, take into account the finiteness of the potential barriers, leading to some weakening of the quantum confinement and, as a consequence, to a more complicated and less steep size-dependence of $\Delta\varepsilon_g(R)$ other than R^{-2}. In addition, electron-hole Coulomb interaction contributes a further $-R^{-1}$ dependence in the blue-shift energy. Both these mechanisms result in a more gradual dependence of the optical gap on the dot radius, which is in fact observed in experiments.

At the same time, low-energy PL with photon energies less than the gap of bulk silicon are also observed in experiments, see, for example, [57]. In this work an extra luminescence peak arose at about 0.9 eV at low temperatures, and its position remained almost unchanged for nanocrystals of various sizes. This may be indeed treated as an attribute of the surface states which can appear inside the band gap of bulk silicon. This possibility and the associated pair-wise trapping rates have been discussed and derived theoretically by Lannoo et al. [58].

2.2. Decay rate

Time-resolved studies of the PL of silicon NCs demonstrate near-exponential decays of the photoluminescence intensity. Typical decay times τ_{PL} vary within a wide range of about 1 to1000 μs depending on the particle size, temperature, detected wavelength, method of preparation, and so forth [31, 32, 51, 59–62]. Such lifetimes are indeed large, and this is an explicit indication of an indirect-band-gap material. Contrary to direct-gap III-V or II-VI compounds, the drop of luminescence intensity for silicon crystallites is sufficiently slow to result in a low PL irradiance compared to direct-gap NCs, even for comparable quantum efficiencies.

The characteristic time of the PL decay is determined by two different recombination mechanisms: radiative, with typical time τ_R; and nonradiative, with typical time τ_{NR}. The rate of the photoluminescence decay is the sum of the radiative and nonradiative recombination rates: $1/\tau_{\mathrm{PL}} = 1/\tau_R + 1/\tau_{\mathrm{NR}}$. In the case where one of the two times is much less than the other, the photoluminescence lifetime coincides with the smallest time. Usually in silicon, the nonradiative channel turns out to be faster compared to the radiative one (see, e.g., [31]), so that the PL lifetime equals τ_{NR}. The quantum yield η, which is proportional to the PL intensity, may be defined as the "weight" of the radiative channel in the recombination process: $\eta = \tau_R^{-1}/\tau_{\mathrm{PL}}^{-1}$. If $\tau_R \gg \tau_{\mathrm{NR}}$, then $\eta = \tau_{\mathrm{NR}}/\tau_R \ll 1$. Obviously, one can use two physically different ways to increase η. The first one is an increase of the radiative transitions, while the second is a decrease of the nonradiative processes. The second way appears easier in practice because the nonradiative processes can be influenced by preparation conditions, as has been recently demonstrated by Miura et al. [62]. On the contrary, according to [62], radiative recombination cannot be controlled by the preparation conditions. Therefore, control of the radiative channel efficiency seems to be fairly difficult to achieve in practice.

Sometimes, both radiative and nonradiative channels contribute comparably in the interband recombination in silicon nanocrystals. In these cases the quantum efficiency becomes very high—possibly on the order of tens of percent [62]. It should be noted, however, that these situations are possible, presumably, at pumping levels corresponding to no more than one excited carrier in every quantum dot. Then, traps such as surface defects may be the main sources of nonradiative recombination. Alternatively, when the excitation power is very high and several electrons are excited in the dots, the Auger process becomes possible. Since Auger interactions are fast, the radiative channel will be "shunted" in this case. Accordingly, η tends to some small value, on the order of a fraction of a percent.

In cases when the nonradiative channel is mostly "closed," that is, $\tau_R \ll \tau_{\mathrm{NR}}$, silicon nanocrystals demonstrate strong temperature dependence of the PL lifetime [23, 33, 57, 63, 64]. In particular, the lifetime becomes smaller as the temperature decreases from ~300 to 4 K. This behavior is explained within the framework of the singlet-triplet two-level model suggested by Calcott et al. [3, 4] for porous silicon. According to this model the exciton state splits due to the electron-hole exchange interaction into the upper singlet with relatively short lifetime $\tau_\uparrow$, and lower triplet with about 2-3 orders-of-magnitude longer lifetime $\tau_\downarrow$. The decay rate is then defined by

$$\frac{1}{\tau_{\mathrm{PL}}} \approx \frac{1}{\tau_R} = \frac{(3/\tau_\downarrow) + (1/\tau_\uparrow)\exp\left[-(\Delta_{\mathrm{S\text{-}T}}/kT)\right]}{3 + \exp\left[-(\Delta_{\mathrm{S\text{-}T}}/kT)\right]}, \tag{1}$$

where $\Delta_{\mathrm{S\text{-}T}}$ is the energy of the singlet-triplet splitting, k is the Boltzmann constant, and T is the temperature. The energy of the singlet-triplet splitting depends on the nanocrystal size and increases from a few meV to 10–20 meV for photon energies increasing from 1.4 eV to 2.2 eV [57, 64]. At low temperature, when $\Delta_{\mathrm{S\text{-}T}} \gg kT$ the decay of the singlet state is strongly suppressed, and the total lifetime τ_{PL} coincides with the longer time $\tau_\downarrow$. In the opposite case (when $\Delta_{\mathrm{S\text{-}T}} \ll kT$), τ_{PL} is close to $4\tau_\uparrow$. As a result, the PL decay occurs substantially faster at low temperature. More rigorous theoretical analysis [65–68] reveals a rich fine structure in the excitonic spectrum of silicon NCs. Exciton states with different symmetry may be ascribed to so-called bright and dark excitons which have essentially different recombination lifetimes.

2.3. Enhancement and quenching of photoluminescence due to impurities

During the past decade, doping Si NCs with shallow impurities has been explored as a potential route for modifying the luminescent properties of silicon nanocrystals. The main

questions are the following: are we able to improve the emission of silicon quantum dots by incorporating donors or acceptors (or both)? If so, then the next question is what is the mechanism for the improvement? The results obtained by different research groups indicate that the PL spectra of silicon nanocrystals are, indeed, sensitive to doping. However, both an increase [10–13] and a decrease [18] of the PL intensity have been observed. This, again, depends on the sample fabrication method and the type of doping.

Silicon NCs doped with phosphorus [10–13, 16, 69], boron [18], or co-doped with P and B [14, 15, 17] have recently been investigated. At the same time, the authors of [70–72] reported on experiments with silicon NCs doped not only with phosphorus or boron but also with hydrogen and nitrogen. Summarizing the results, one can conclude that doping with phosphorus or codoping with phosphorus and boron can enhance the PL intensity of the nanocrystals by several times, as initially reported in [10]. Meanwhile, no enhancement is observed for NCs doped with boron, hydrogen, or nitrogen. Moreover, the degree of quenching of the luminescence depends on the annealing procedure [18, 70–72].

In accordance with the results of Miura et al. [12], Fujii et al. [13], and Mikhaylov et al. [72] reported that an increase of the phosphorus concentration leads to an initial rise of the photoluminescence peak, whereupon the PL intensity subsequently decreases with a further increase in doping. Moreover, the P concentration corresponding to the maximum intensity becomes greater with decreasing NC size [11–13]. Therefore, in some cases, where the NCs had small sizes of about 3-4 nm [11, 70], only a monotonic rise of the PL peak was observed as P concentration increased. One possible reason for this phenomenon lies in the passivation of dangling bonds (i.e., neutral or charged P_b centers) at the NC surfaces. The absence of the enhancement effect for heavily P-doped crystallites at a given size has been explained by more extensive Auger recombination [14, 15, 17] or a coalescence mechanism [72]. The authors of [72] also pointed out the essential distinction in the photolumine scence of the P-doped nanocrystals formed by ion implantation at 1000°C and 1100°C. The former demonstrate up to 5 to 6 times intensity enhancement, while for the latter ony PL quenching was found (Figure 3).

As a method to reduce the Auger recombination, simultaneous codoping with phosphorus and boron, thereby compensating the numbers of donors and acceptors inside the crystallite, has been proposed [14, 15, 17]. PL enhancement was successfully obtained for larger nanocrystals of ~6–8 nm in diameter. In this case, a large shift of the PL peak, even below the optical gap of bulk silicon, takes place when increasing P concentration with fixed concentration of boron [14]. This may be evidence of the formation of bulk-like impurity states. At the same time, codoping with high concentration of both donor- and acceptor-type impurities result in a strong chemical shift of the ground-state energy levels in the conduction and valence bands [73], which may substantially reduce the NC optical gap. In the latter case no assumptions on the bulk-like form of electron states in silicon quantum dots are required, because the effect of the strong chemical shift is exclusively due to the confining potential of the dot.

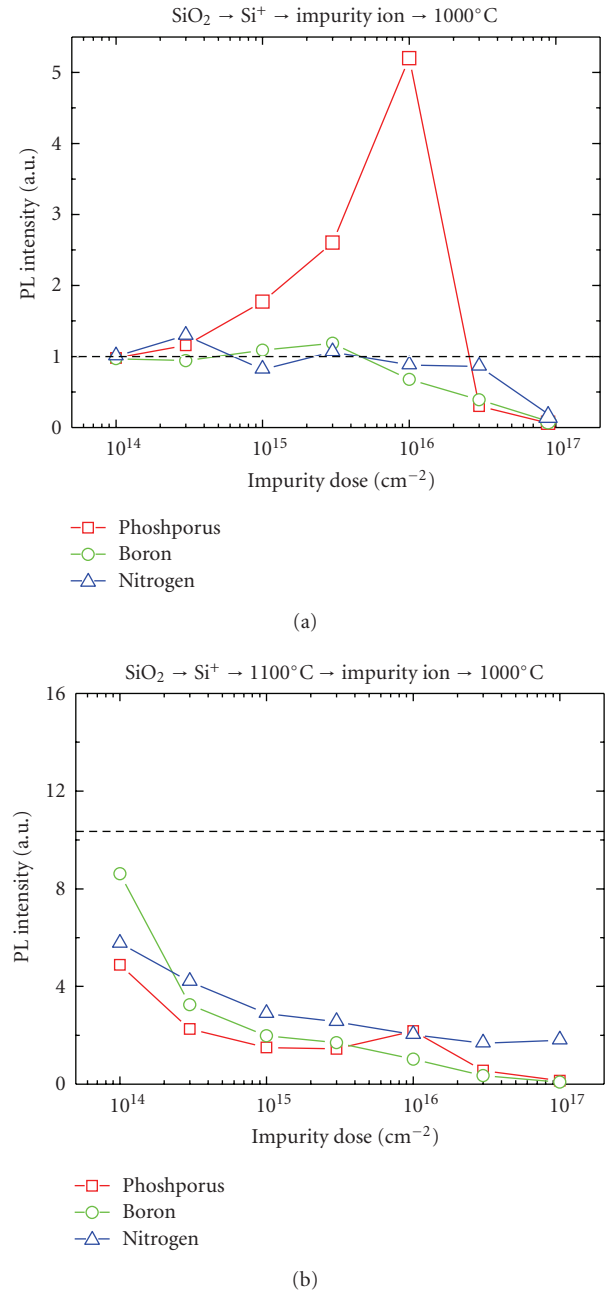

Figure 3: Influence of doping with P, B, N on the PL intensity at 750 nm in Si NC layers synthesized by ion implantation and annealed at either 1000 or 1100°C. Samples were subsequently implanted with impurity ions and then re-annealed. The dashed line represents the intensity of the undoped reference sample. (The figures have been kindly provided by D. I. Tetelbaum, A. N. Mikhaylov, O. N. Gorshkov, D. I. Kambarov, V. K. Vasiliev, and A. I. Belov, who did the experiments).

3. SINGLE-DOT PROBLEM

We next turn to the quantum-mechanical analysis of various aspects of light emission in silicon nanocrystals. It is quite clear, of course, that a consideration of electronic structure, electron-hole recombination, and the role of impurities in a single quantum dot provides a basis for understanding optical properties of the quantum-dot ensembles. Therefore the present chapter first discusses some theoretical models concerning the interband transitions in an individual quantum dot. First, we will discuss the optical gap and energy spectra of undoped nanocrystals. Then the "band" structure and charge distribution in doped dots will be analyzed. Finally, the recombination lifetimes will be calculated for undoped and doped crystallites.

3.1. *Electronic structure of perfect silicon nanocrystals*

The first step is a calculation of the ground-state energies both for the conduction and valence bands of a nanocrystal. Note that here and throughout the paper we will use terminology that is typical for the bulk material. Of course, no genuine energy bands exist in the nanocrystal because of its finite size. Nevertheless, the states above and below the NC optical gap originate from the size-quantized states of conduction and valence bands of the bulk crystal, respectively. Moreover, in the following we mainly intend to employ the envelope-function approximation ($\mathbf{k}\cdot\mathbf{p}$ method) to describe electronic states of the nanocrystals. Consequently, such the terminology is convenient and should not lead to any misunderstandings. The states above and below the optical gap will be further referred to as conduction and valence bands, as in the bulk. Different approaches are used when calculating the gap of silicon nanocrystals. Among them, the simplest is the single-particle approximation. Usually, the single-particle gap exceeds real optical gap because the electron-hole Coulomb interaction reduces the total energy of the system. For this reason, the values of the single-particle gap may be treated as an upper bound for the optical gap. In this section we discuss electron and hole states of a "pure" crystallite, which has no defects and a perfect diamond lattice all over its whole volume. The results are compared with the simpler approximations discussed in the introduction.

3.1.1. *Optical gap. Numerical results*

It is possible to separate all calculation methods applied for computation of the electronic spectra in pure NCs into two groups. In the first group we have the numerical first-principles, empirical, and semi-empirical methods, such as density functional theory (DFT) [68, 74–78], pseudopotential (PP) method (or various combinations of PP and DFT) [79–82], tight-binding (TB) models [83–86], combined Green's function (GW-approximation), and the Bethe-Salpeter equation (BSE) technique [87–89]. All these methods require considerable computational time, a problem that worsens as the nanocrystal size is increased. Analytical methods such as the effective mass approximation or $\mathbf{k}\cdot\mathbf{p}$ method [67, 90–95] may be ascribed to the second group. In following we combine these two methods into a single envelope function approximation (EFA). The latter allows one to perform calculations without any restrictions on cluster sizes. Additionally, this approach can be used to find the higher excited states of the nanocrystal.

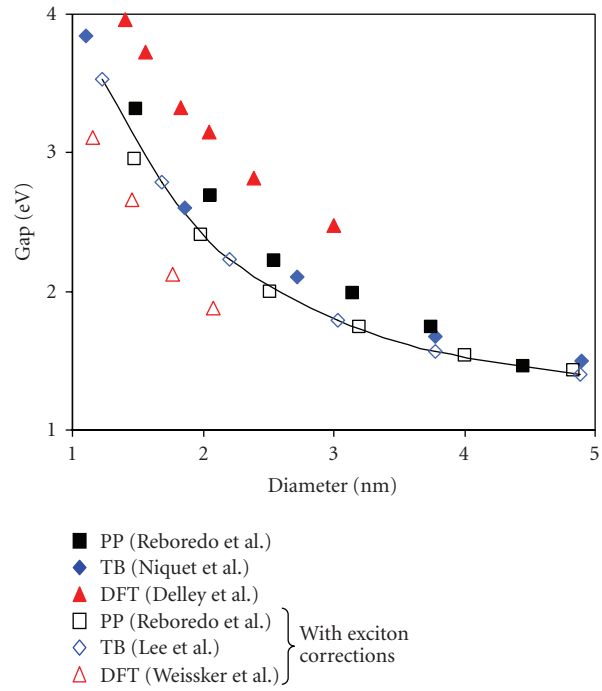

FIGURE 4: Optical gap calculated by PP [65], TB [85, 86], and DFT [68, 74] methods. Solid line: EFA calculations, see (22) below [93].

In the present subsection, we summarize the results of some of the methods discussed above, which illustrate dependence of the optical gap on the nanocrystal size (Figure 4). In all calculations, any dangling bonds at the nanocrystal surface were considered to be H-passivated. As is seen in the figure, there is some scatter of data due to the different computational methods and different approximations utilized in the computational procedure.

In particular, taking into account the self-energy correction or electron-hole interaction can considerably change the magnitude of the nanocrystal optical gap, in opposite directions, as has been pointed out by many authors (see, e.g., [81, 88, 89]). In particular, it is known that the local density approximation of the DFT tends to underestimate the optical-gap (similar results happen for silicon nanowires) [96, 97] compared to those obtained in experiments. For a more accurate account of the self-energy corrections and excitonic effects, the GW+BSE approach is often applied. The combination of the GW and BSE methods yields almost complete compensation of the exciton and the self-energy corrections to the single-particle optical gap [88]. The same effect was also found by Franceschetti and Zunger [81] within the framework of the PP method. Unfortunately, the GW+BSE approach is employed for nanocrystals whose diameters do not exceed 1 nm [87–89]. Therefore, we did not depict the results of this approach in Figure 4.

3.1.2. Electron and hole spectra in a dot

Let us now discuss electronic spectra in both the valence and conduction bands of the quantum dot. As has been pointed out, for this purpose it is convenient to use the EFA. Here we describe in more detail not only the lowest but also the higher excited electronic states as a function of size.

We assume the total potential energy of the electron inside the quantum dot to be of the following form

$$U(\mathbf{r}) = U_0(r) + V_{\mathrm{sp}}(r). \tag{2}$$

Here $U_0(r)$ is the confining potential equal to zero inside and infinity outside the dot. The second part $V_{\mathrm{sp}}(r)$ describes an interaction between the electron and its image, arising due to the charge polarization on the boundary between the silicon nanocrystal and its dielectric surrounding. $V_{\mathrm{sp}}(r)$ is often referred to as a self-polarization term. It can be represented as

$$V_{\mathrm{sp}}(r) = \frac{e^2(\varepsilon_s - \varepsilon_d)}{2\varepsilon_s R}\sum_{l=0}^{\infty}\frac{l+1}{l\varepsilon_s + (l+1)\varepsilon_d}\frac{r^{2l}}{R^{2l}}, \tag{3}$$

where ε_s and ε_d are the static dielectric constants of silicon and the dielectric matrix, respectively. In order to find the electronic states in the dot, we have to solve the single-particle Schrödinger-like equation for the envelope function vector $|\Phi\rangle$:

$$(H + U(\mathbf{r}))|\Phi\rangle = E|\Phi\rangle. \tag{4}$$

Here, H is the bulk $\mathbf{k}\cdot\mathbf{p}$ Hamiltonian operator acting on the six-dimensional (6D) envelope-function vectors $|\Phi\rangle$, and E is the electron energy. The components of the 6D-vector $|\Phi\rangle$ are slowly varied expansion coefficients $\Phi_j(\mathbf{r})$ of the total wave function in the Bloch-state basis.

The electronic states in the valence and conduction bands can be determined separately. Starting with the valence band, the Bloch-state for the Γ-point is $|YZ\rangle|\uparrow\rangle$, $|XZ\rangle|\uparrow\rangle$, $|XY\rangle|\uparrow\rangle$, $|YZ\rangle|\downarrow\rangle$, $|XZ\rangle|\downarrow\rangle$, $|XY\rangle|\downarrow\rangle$, where $|\uparrow\rangle$ and $|\downarrow\rangle$ are "up" and "down" spinors, respectively, and the Bloch functions $|YZ\rangle$, $|XZ\rangle$, $|XY\rangle$ belong to the irreducible representation $\Gamma_{25'}$. The $\mathbf{k}\cdot\mathbf{p}$ Hamiltonian matrix H in 4 is the sum of three parts: $H = H^{(0)} + H^{(1)} + H^{(\mathrm{so})}$. Here $H^{(0)} = (\mathbf{p}^2/2m_h)\times\mathbf{I}$ is the isotropic part obtained as the average of the total $\mathbf{k}\cdot\mathbf{p}$ matrix over all angles in $\mathbf{p}$-space. $H^{(1)}$ is the anisotropic part that can be represented by two equivalent 3×3 blocks situated on the main diagonal of the total 6×6 $\mathbf{k}\cdot\mathbf{p}$ matrix:

$$H^{(1)} = \begin{pmatrix} H_3 & 0 \\ 0 & H_3 \end{pmatrix},$$
$$H_3 = -\frac{1}{2m_0}\begin{pmatrix} Q_1 & Np_xp_y & Np_xp_z \\ Np_xp_y & Q_2 & Np_yp_z \\ Np_xp_z & Np_yp_z & Q_3 \end{pmatrix}, \tag{5}$$

where Q_1 denotes $((L-M)/3)(3p_x^2 - \mathbf{p}^2)$, Q_2 denotes $((L-M)/3)(3p_y^2 - \mathbf{p}^2)$, and Q_3 denotes $((L-M)/3)(3p_z^2 - \mathbf{p}^2)$.

Finally, the term

$$H^{(\mathrm{so})} = \frac{1}{3}\begin{pmatrix} 0 & -i\Delta & 0 & 0 & 0 & \Delta \\ i\Delta & 0 & 0 & 0 & 0 & -i\Delta \\ 0 & 0 & 0 & -\Delta & i\Delta & 0 \\ 0 & 0 & -\Delta & 0 & i\Delta & 0 \\ 0 & 0 & -i\Delta & -i\Delta & 0 & 0 \\ \Delta & i\Delta & 0 & 0 & 0 & 0 \end{pmatrix} \tag{6}$$

describes the spin-orbit interaction. We have introduced above the spin-orbit energy Δ equal to 44 meV for silicon, the 6×6 identity matrix $\mathbf{I}$, and the hole effective mass $m_h = 3m_0/(L+2M)$, where the numbers L, M, N are dimensionless empirical parameters in the $\mathbf{k}\cdot\mathbf{p}$ Hamiltonian operator in the valence band. For silicon they equal 5.8, 3.43, and 8.61, respectively [98].

Because of the isotropic and diagonal form of the operator $H^{(0)} + U_0(r)$, it is possible to classify its eigenstates similarly to atomic systems using common terminology such as s-, p-, and d-type states, and so forth [92]. Accordingly, one may expand the components of the envelope-function vectors over these eigenstates as

$$\Phi_j(\mathbf{r}) = \sum_{\alpha} C_{j\alpha}|\alpha\rangle, \tag{7}$$

where $|\alpha\rangle$ stands for the s-, p-, d-, ... states and $C_{j\alpha}$ are the expansion coefficients. For instance, the $1s$-, $1p$-, $1d$-, (in the following simply s-, p-, and d-) and $2s$-type states are described by the following functions:

$$\begin{aligned}
|s\rangle &= \sqrt{\frac{\pi}{2R^3}}\, j_0(\pi r/R), \\
|p_a\rangle &= \sqrt{\frac{3}{2\pi R^3}}\,\frac{j_1(\mu_1 r/R)}{j_0(\mu_1)}\,\frac{x_a}{r}, \\
|d_{ab}\rangle &= \sqrt{\frac{15}{2\pi R^3}}\,\frac{j_2(\mu_2 r/R)}{j_1(\mu_2)}\,\frac{x_a x_b}{r^2}, \quad a\neq b, \\
|d_{x^2-y^2}\rangle &= \sqrt{\frac{15}{8\pi R^3}}\,\frac{j_2(\mu_2 r/R)}{j_1(\mu_2)}\,\frac{x^2-y^2}{r^2}, \\
|d_{3z^2-r^2}\rangle &= \sqrt{\frac{15}{8\pi R^3}}\,\frac{j_2(\mu_2 r/R)}{j_1(\mu_2)}\,\frac{3z^2-r^2}{r^2}, \\
|2s\rangle &= \sqrt{\frac{\pi}{2R^3}}\, j_0(2\pi r/R),
\end{aligned} \tag{8}$$

where $j_n(x)$ are the spherical Bessel functions of argument x, and μ_n are the first roots of $j_n(x)$. Below, we restrict the basis of envelope functions $|\alpha\rangle$ with these states only, and determine the electron and hole spectra. Substitution of $\Phi_j(\mathbf{r})$ into (4) yields algebraic equations for $C_{j\alpha}$:

$$(E - E_\alpha)C_{i\alpha} = \sum_{\beta}\langle\alpha|H_{ij}^{(1)} + H_{ij}^{(\mathrm{so})} + V_{\mathrm{sp}}(\mathbf{r})\delta_{ij}|\beta\rangle C_{j\beta}, \tag{9}$$

where E_α denotes the energy of the state $|\alpha\rangle$, δ_{ij} stands for the Kronecker delta, and the Einstein convention has been used

when summing over j. Considering all operators in the right side of (9) as perturbations [92], one can solve the equation and find the energies in the valence band.

Restricting the basis of the envelope states $|\alpha\rangle$ by $1s$, $2s$, $1p$, and $1d$ functions, and neglecting the spin-orbit interaction, we obtain the following "hierarchy" of energies (for convenience, we write down the hole energies differing in the sign from the electron energies, which are determined with (9)). The ground-state energy

$$E_h^{(s)} = \frac{\hbar^2\pi^2}{2m_hR^2} \tag{10}$$

is triply degenerate (or sixfold, if spin is taken into account). It is the energy of the $1s$ state. Hybridization of the p-type states yields four different levels with the energies

$$\begin{aligned}
E_{h1}^{(p)} &= \frac{\hbar^2\mu_1^2}{2m_hR^2}\left[1 - \frac{3N+2L-2M}{5L+10M}\right],\\
E_{h2}^{(p)} &= \frac{\hbar^2\mu_1^2}{2m_hR^2}\left[1 - \frac{3N-4L+4M}{5L+10M}\right],\\
E_{h3}^{(p)} &= \frac{\hbar^2\mu_1^2}{2m_hR^2}\left[1 + \frac{3N-2L+2M}{5L+10M}\right],\\
E_{h4}^{(p)} &= \frac{\hbar^2\mu_1^2}{2m_hR^2}\left[1 + \frac{6N+4L-4M}{5L+10M}\right],
\end{aligned} \tag{11}$$

where $\mu_1 = 4.4934$. The energies of the d-d hybridized states are as follows:

$$\begin{aligned}
E_{h1}^{(d)} &= \frac{\hbar^2\mu_2^2}{2m_hR^2}\left[1 - \frac{6N}{7L+14M}\right],\\
E_{h2}^{(d)} &= \frac{\hbar^2\mu_2^2}{2m_hR^2}\left[1 - \frac{3N+4L-4M}{7L+14M}\right],\\
E_{h3}^{(d)} &= \frac{\hbar^2\mu_2^2}{2m_hR^2}\left[1 + \frac{3N-2L+2M}{7L+14M}\right],\\
E_{h4}^{(d)} &= \frac{\hbar^2\mu_2^2}{2m_hR^2}\left[1 + \frac{6N-4L+4M}{7L+14M}\right],
\end{aligned} \tag{12}$$

where $\mu_2 = 5.7634$. Finally, the energies of the $1d$-$2s$ hybrids are written as

$$\begin{aligned}
E_{h1}^{(2sd)} &= \frac{\hbar^2}{2m_hR^2}\left[\frac{4\pi^2+\mu_2^2}{2} + \frac{3\mu_2^2}{14}\frac{N+2L-2M}{L+2M}\right.\\
&\qquad \left. - \frac{12\sqrt{6}}{\sqrt{5}}\frac{\pi\mu_2}{4\pi^2-\mu_2^2}\frac{N}{L+2M}\right],\\
E_{h2}^{(2sd)} &= \frac{\hbar^2\mu_2^2}{2m_hR^2},\\
E_{h3}^{(2sd)} &= \frac{\hbar^2}{2m_hR^2}\left[\frac{4\pi^2+\mu_2^2}{2} + \frac{3\mu_2^2}{14}\frac{N+2L-2M}{L+2M}\right.\\
&\qquad \left. + \frac{12\sqrt{6}}{\sqrt{5}}\frac{\pi\mu_2}{4\pi^2-\mu_2^2}\frac{N}{L+2M}\right].
\end{aligned} \tag{13}$$

The contribution of the self-polarization term from (10)–(13) has been omitted since it represents, in fact, a common shift of all the levels by $e^2(1/\varepsilon_d - 1/\varepsilon_s)/2R$.

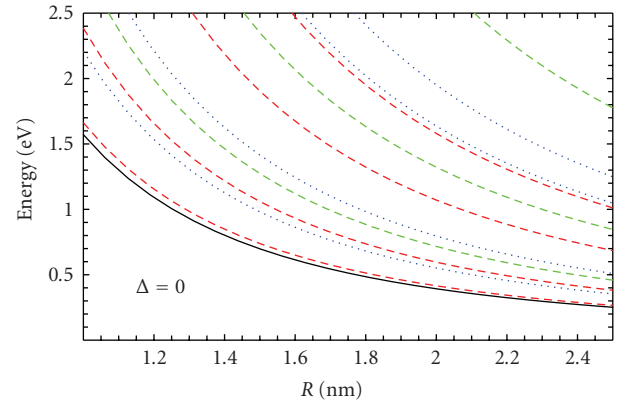

Figure 5: Hole energy spectrum according to (10)–(13) in case of no spin-orbit interaction. Solid line: s-type level. Short dashed lines: p-p hybridized levels. Dots: d-d hybridized levels. Long dashed lines: $2s$-d hybridized levels. All energies are counted deep into the valence band with respect to the valence band maximum. The degeneracy degree including spin (from bottom to top) is 6; 6; 6; 4; 6; 4; 6; 6; 2; 6; 2; 6.

In Figure 5 the energy levels from (10)–(13) have been plotted as functions of the NC radius. The two lowest hole levels have very similar energies. The lowest level, being sixfold degenerate, corresponds to six electron states with an s-type envelope function. These states have an isotropic macroscopic (averaged over the unit-cell volume) charge distribution inside the dot. The second level corresponds to six electron states with p-type envelope functions. Correspondingly, the macroscopic charge has an anisotropic distribution for these states (see [92] for details).

In the conduction band the Bloch-state basis consists of six Bloch functions of three different X-points in the Brillouin zone [99]. We denote three pairs of these functions as $|X\rangle$, $|X'\rangle$; $|Y\rangle$, $|Y'\rangle$; $|Z\rangle$, $|Z'\rangle$. Each pair belongs to the twofold degenerate irreducible representation X_1 of the corresponding X-point. The unprimed Bloch functions have a nonzero value at the lattice site, while the primed functions are zero at those points. The choice of the X_1-functions as the Bloch basis allows us to describe correctly a dispersion-law nonparabolicity that originates mainly from the energy-branch crossing in the X-points.

The $\mathbf{k}\cdot\mathbf{p}$ Hamiltonian operator in the conduction band represents a 6×6 matrix having the form

$$H = \begin{pmatrix} H_x & 0 & 0\\ 0 & H_y & 0\\ 0 & 0 & H_z \end{pmatrix}. \tag{14}$$

Each element of the matrix H is a block 2×2 matrix defined by the following expressions [99]:

$$H_a = \begin{pmatrix} \dfrac{p_a^2}{2m_l} + \dfrac{\mathbf{p}^2-p_a^2}{2m_t} & \left(\dfrac{1}{m_t}-\dfrac{1}{m_0}\right)p_bp_c + i\dfrac{p_0}{m_l}p_a\\[2ex] \left(\dfrac{1}{m_t}-\dfrac{1}{m_0}\right)p_bp_c - i\dfrac{p_0}{m_l}p_a & \dfrac{p_a^2}{2m_l} + \dfrac{\mathbf{p}^2-p_a^2}{2m_t} \end{pmatrix}. \tag{15}$$

Here $p_0 \approx 0.14(2\pi\hbar/a_0)$ is the distance in $\mathbf{p}$-space from any of the energy minima to the nearest X-point, a_0 is the lattice constant of silicon. $m_l = 0.92m_0$ and $m_t = 0.19m_0$ are the "longitudinal" and "transverse" effective masses. The origin of the E-axis coincides with the X-point energy. Each of the small indices (a, b, c) runs over the values x, y, or, z and always differs from the others.

Solving (4) for the conduction band is done in the same way as for the valence band, as in (9)–(13) above. One can then obtain the following groups of energies. The ground states, as well as the second excited ones, are the $1s$-$1p$ hybrids. Their energy levels are given by

$$E_{e1}^{(sp)} = \frac{E_s + E_p - 2H_{pp}}{2} - \sqrt{\left(\frac{E_p - E_s - 2H_{pp}}{2}\right)^2 + H_{sp}^2},$$
$$E_{e2}^{(sp)} = \frac{E_s + E_p - 2H_{pp}}{2} + \sqrt{\left(\frac{E_p - E_s - 2H_{pp}}{2}\right)^2 + H_{sp}^2}, \tag{16}$$

where

$$H_{sp} = \frac{ip_0}{m_l}\langle s \,|\, p_z \,|\, p_z\rangle = \frac{2\pi\hbar\mu_1 p_0}{[\sqrt{3}m_l R(\mu_1^2 - \pi^2)]},$$
$$H_{pp} = \frac{1}{12}\left(\frac{1}{m_t} - \frac{1}{m_l}\right)\langle p_z \,|\, \mathbf{p}^2 - 3p_z^2 \,|\, p_z\rangle = \frac{\hbar^2\mu_1^2(m_l - m_t)}{15m_t m_l R^2} \tag{17}$$

are s-p and p-p type matrix elements of anisotropic part H_a, $E_s = \hbar^2\pi^2/2m_eR^2$, and $E_p = \hbar^2\mu_1^2/2m_eR^2$ are the energies of the s- and p-type states of the isotropic unperturbed Hamiltonian operator. The isotropic average electron effective mass is defined by $m_e^{-1} = (2m_t^{-1} + m_l^{-1})/3 \approx (0.26m_0)^{-1}$. The p-p hybridization forms states with energies:

$$E_{e1,2}^{(p)} = E_p + H_{pp} \mp H_{xy}. \tag{18}$$

Here $H_{xy} = \hbar^2\mu_1^2(m_0 - m_t)/5m_t m_0 R^2$. The next three levels are the result of the d-d hybridization:

$$E_{e1}^{(d)} = \frac{\hbar^2\mu_2^2}{2m_eR^2}\left(1 - \frac{2}{7}\frac{m_l - m_t}{2m_l + m_t} - \frac{6}{7}\frac{m_l}{m_0}\frac{m_0 - m_t}{2m_l + m_t}\right),$$
$$E_{e2}^{(d)} = \frac{\hbar^2\mu_2^2}{2m_eR^2}\left(1 + \frac{4}{7}\frac{m_l - m_t}{2m_l + m_t}\right), \tag{19}$$
$$E_{e3}^{(d)} = \frac{\hbar^2\mu_2^2}{2m_eR^2}\left(1 - \frac{2}{7}\frac{m_l - m_t}{2m_l + m_t} + \frac{6}{7}\frac{m_l}{m_0}\frac{m_0 - m_t}{2m_l + m_t}\right).$$

Finally, the $2s$-d hybridized energies are obtained numerically:

$$E_{e1}^{(2sd)} = \frac{\hbar^2}{2m_eR^2}\left(\frac{4\pi^2 + 2\mu_2^2}{3} - 0.477\mu_2^2\right),$$
$$E_{e2}^{(2sd)} = \frac{\hbar^2}{2m_eR^2}\left(\frac{4\pi^2 + 2\mu_2^2}{3} - 0.455\mu_2^2\right), \tag{20}$$
$$E_{e3}^{(2sd)} = \frac{\hbar^2}{2m_eR^2}\left(\frac{4\pi^2 + 2\mu_2^2}{3} + 0.932\mu_2^2\right).$$

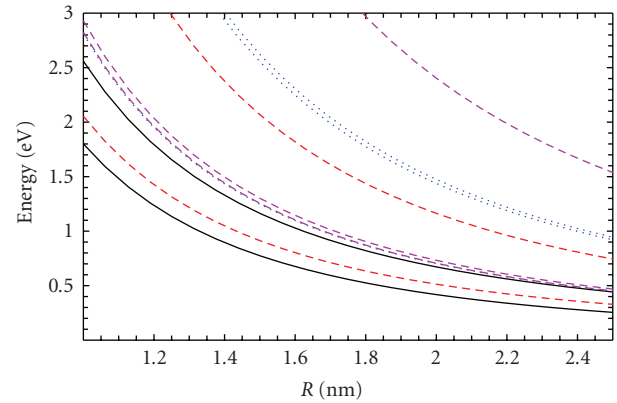

Figure 6: The lowest energy levels in the conduction band as functions of the NC radius, from (16)–(20). The energies are counted from the X-point energy. Solid line: s-p type levels. Short dashed lines: p-p hybridized levels. Dots: d-d hybridized levels. Long dashed lines: $2s$-d hybridized levels. All the levels are 12-fold degenerate including spin degeneracy.

The results for the single-particle electron spectrum in the conduction band are shown in Figure 6.

The wave function of the ground state turns out to be a superposition of the terms with s- and p-type envelope functions (see [92] for details). The "weight" of the s-type envelope function is greater than that of the p-type function. Therefore the macroscopic charge for the ground state has a distribution close to isotropic.

From the above calculations, the optical gap of the NC can be obtained as the sum of the lowest energies in both bands and the energy difference between X- and Γ-points in bulk $\Delta_{X\Gamma} = 1.24$ eV:

$$\varepsilon_g(R) = \Delta_{X\Gamma} + E_{el}^{(sp)} + E_h^{(s)}. \tag{21}$$

This energy somewhat overestimates value compared to that obtained with the numerical methods, as indicated by the solid line in Figure 7. This is a consequence of two main factors.

The first factor is that we have assumed infinitely high potential barriers at the interface. The authors of [91, 93, 95] calculated the carrier energies supposing the potential barriers to be finite and equal to approximately 3 eV (or a little more) for electrons and 4-5 eV for holes. Moreover, the discontinuity of the effective mass has been taken into account. In Figure 7 we have plotted the optical gap of silicon nanocrystal versus the confining parameter $1/R$ for three models differeing according the nanocrystal's surroundings. The solid line corresponds to infinitely high potential barriers. Circles represent the finite barriers and constant effective mass throughout the sample. Finally, in case of the mass discontinuity with effective mass outside the dot coinciding with free electron mass, the optical gap has been represented by disks. For the last two cases, the dependence $\Delta\varepsilon_g(R)$ becomes weaker than R^{-2}, especially for the case of the discontinuous effective mass where the dependence is

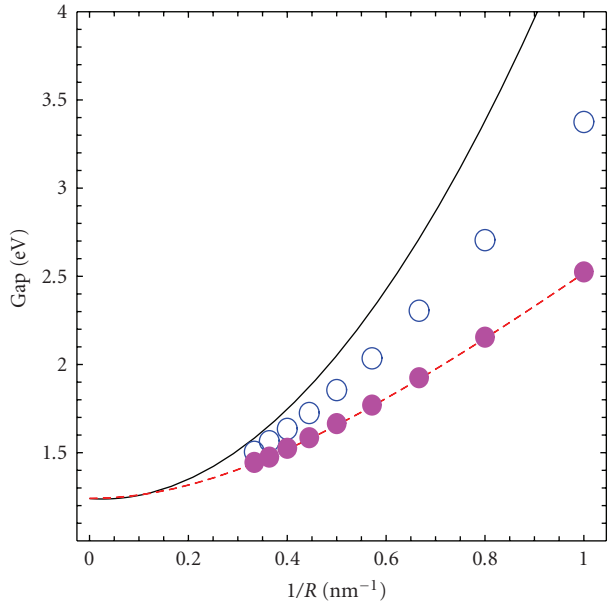

FIGURE 7: NC gap versus reciprocal dot radius. Solid line: infinite barriers (21). Circles: finite barriers (3.2 eV for electrons and 4.3 eV for holes, which corresponds to Si/SiO_2 interface) and constant effective mass. Disks—finite barriers and free electron mass outside the dot. Both of the latter are numerical results by EFA [92]. The dashed line is a guide to the eye.

closer to $1/R$. In the last case the gap dependence is well fitted by the function:

$$\varepsilon_g^{(1)}(R) = \sqrt{{\varepsilon_g}^2 + \frac{D_1}{R^2}} \tag{22}$$

with $D_1 = 4.8\,\text{eV}^2\cdot\text{nm}^2$. In general, one may conclude that the calculated values of the optical gap are reduced due to the barrier finiteness and mass discontinuity, and agree better with those shown in Figure 4.

The second factor, strongly influencing the dot gap, is electron-hole Coulomb interaction. Its contribution to the optical gap will be discussed in the next subsection.

3.1.3. EFA calculations: exciton corrections

The electron-hole interaction reduces the energy of the electron-hole pair. As a result, the exciton optical gap is also reduced. In order to estimate the exciton correction to the total electron-hole single-particle energy one must solve the two-particle problem. This has been done for silicon NCs embedded in an infinitely wide-band-gap material [67, 90, 94]. The exciton corrections were found to be about 0.4 eV [67], 0.25 eV [90], and 0.3 eV [94] for 2-nm-diameter NCs, with the correction decreasing approximately as R^{-1} with increasing size.

Meanwhile, as has been pointed out in the preceding section, the finiteness of the potential barriers and effective mass discontinuity can appreciably influence the electron and hole energies. Therefore, it is possible to expect the same for the excitonic energies. Ferreyra and Proetto [91] have studied excitonic states for a quantum dot in vacuum. Accordingly, they accepted the barrier heights equal to the electron affinity of the corresponding bulk material for electrons and infinity for holes, and the effective mass being m_0. They found an exciton correction of the order of 0.2 eV for a 2-nm-diameter dot. As the nanocrystal size increases, the magnitude of this correction decreased as $R^{-0.7}$.

The authors of some of the previous work (e.g., [67, 90, 91]) treated the Coulomb potential energy as $V_C = -e^2/\varepsilon_s r_{\text{eh}}$ similar to bulk silicon. However, in a quantum dot the electron and hole interact not only with each other but also with their "images" due to the difference in the permittivity of the materials inside and outside the dot. These are the so-called polarization fields arising because of the charge polarization at the dot boundary. The interaction with the polarization fields has been taken into account in [94]. Nevertheless, the polarization fields did not lead to any significant corrections to the optical gap. As mentioned above, the correction does not exceed 0.3 eV, which is close to the values obtained by other authors.

Evidently, the calculations carried out with the EFA [67, 90, 91, 94] provide sufficiently good coincidence with both experimental and theoretical data. For comparison, we have depicted in Figure 4 with the solid line the EFA single-particle gap according to (22). The gap values $\varepsilon_g^{(1)}(R)$ agree well with those computed by PP, TB, and DFT methods. Obviously, a small exciton correction of about 0.3–0.1 eV for 2 to 5 nm diameter crystallites, respectively, does not significantly change the single-particle gap values.

It should be noted, in conclusion, that all the authors employed the perturbation theory considering the electron-hole interaction to be weak compared to the typical quantum confinement energies in the dot. Such an approach is justified if the exciton Bohr radius is significantly larger than the dot radius. This requirement remains valid for small quantum dots with the sizes of about 5-6 nm or less.

3.1.4. Interface states

We have already emphasized in the introduction that radiative transitions between interface states are also often considered as the origin of NIR, or even visible, emission from silicon nanocrystals. In a certain sense, this point of view is alternative to the idea of quantum confinement. Description of the interface states with EFA is difficult because the real potential existing in the vicinity of the nanocrystal surface has in principle a microscopic nature that manifests itself at a distance on the order of a bond length. Meanwhile, the EFA is, in fact, a "macroscopic" method which is not able to distinguish the spatial structure on scales smaller than the size of the primitive cell. Therefore TB and DFT methods are essentially more suitable for this goal.

As a rule, interface states originate from various-type defects existing at the surface of the crystallite. These include, mainly, dangling bonds (P_b centers) which can be neutral, positively, or negatively charged, and different SiO bonds (backbonded and double bonded oxygen) arising at Si/SiO_2 interface. Charged dangling bonds corresponding to zero or two electrons in the bond level, respectively, produce deep

levels inside the band gap of bulk silicon. Their energies are approximately 0.3 eV below the conduction band minimum for the negatively charged bond, and 0.3 eV above the valence band maximum if the bond is positively charged [100]. Consequently, the effective gap between these levels is about 0.5-0.6 eV [101]. For nanocrystals, the effective gap gradually rises as the nanocrystal size decreases. In particular, for a 5-nm-diameter NC this shift equals approximately 0.6 eV, while for a 2 nm crystallite it is 1.3-1.4 eV [100]. Thus, we see that the dangling bond levels are sensitive to the NC size.

Nanocrystal oxidation has been studied theoretically by TB [8, 102], DFT [103, 104], and GW+BSE [89] methods. The role of the so-called backbonded (Si–O–Si) and double bonded (Si=O) oxygen atoms has been examined for the case where the spherical NC surface is passivated with hydrogen. In the first case (Si–O–Si), oxygen forms two bonds with two different silicon atoms which already have four bonds with other silicon or hydrogen atoms. In the second case (Si=O), oxygen replaces two hydrogen atoms bonded with one silicon atom. It is natural to suppose that the system perturbation in the second case should be more significant because of the stronger distortions of the structure. In fact, it was found that the presence of one Si=O bond at the NC surface provides an optical gap almost independent of the dot size [8]. At the same time, the nanocrystal with a Si–O–Si bond has a gap that gradually decreases with increasing size. Nevertheless, this gap remains smaller, and varies more slowly than the gap of perfect nanocrystal with hydrogen passivated surfaces. The calculations carried out by different methods [89, 102, 103] for oxidized crystallites show an essential difference in the energy of the ground electron-hole transition in crystallites with Si–O–Si and Si=O bonds. All the methods used exhibit the smallest gap for the case of double-bond oxidation, while the crystallites with backbonded oxygen have the greater gap. In turn, the latter is less than the gap of a perfect NC. The authors of [89] have found that only the bridge-type bond (Si–O–Si) can provide a satisfactory agreement with experiments on the photoluminescence in nc-Si/SiO_2 system. This fact may be explained by the considerably different oscillator strengths of the ground transitions for NCs with Si=O and Si–O–Si defects. As has been shown by Nishida [102], the oscillator strength for Si–O–Si case is several orders of magnitude greater than that for Si=O case, especially for NCs smaller than 1 nm in diameter. This is precisely the case studied by Luppi et al. [89], where NCs of 0.5 nm and 0.9 nm in diameter were considered. However, according to [102] the difference between the size-quantized energy levels and those of the Si=O and Si–O–Si defects, as well as the difference in the oscillator strengths of the ground electron-hole transitions, are essential only for NC diameters less than 2 to 2.5 nm [8, 102]. For larger sizes, the energies and the transition intensities for perfect and oxidized crystallites almost coincide.

Finally, nonradiative trapping rates are also critical in the light emission properties of silicon NCs. The group of neutral or charged P_b centers at silicon dangling bonds is the most important nonradiative trap in bulk silicon [105], and acts also in the case of Si NCs [58]. In a detailed theoretical investigation, Lannoo et al. [106] found that the carrier trapping at neutral P_b centers is nonradiative, whereas capture at charged centers can lead to photon emission at energies smaller than the bandgap of bulk silicon. The rate for carrier trapping at a neutral dangling bond defect at the Si–SiO_2 interface in a NC with a single P_b center was established theoretically as a function of the NC size [106]:

$$w_{nr} = \frac{\sigma_0 \nu}{V} \frac{1}{\sqrt{2\pi}} \left(\left(\frac{E_0}{\hbar\omega} \right)^2 + z^2 \right)^{-0.25} \times \exp\left[-S \coth\left(\frac{\hbar\omega}{2kT} \right) + \frac{E_0}{2kT} + \left(\left(\frac{E_0}{\hbar\omega} \right)^2 + z^2 \right)^{0.5} - \frac{E_0}{\hbar\omega} a \sinh\left(\frac{E_0}{\hbar\omega z} \right) \right]. \quad (23)$$

In (23), σ_0 is the capture cross section given by c_0/ν where c_0 is the capture coefficient and ν is the thermal velocity equal to $\sqrt{8kt/\pi m^*}$, E_0 is the ionization energy of the defect (approximately equal to the Franck-Condon energy plus the carrier confinement energy), S is the Huang-Rhys factor ($S = \sim 15$) [107], $\hbar\omega$ is the average phonon energy, V is the nanocrystal volume, and $z = S/[\sinh(\hbar\omega/2kT)]$. The capture rate increases strongly as a function of NC size due to the decreasing defect ionization energy, until eventually the volume term begins to dominate the trapping rate, which then begins to decrease again. Since, the calculated rate is for a single isolated defect, in practice the rate should be modified for the likelihood of multiple defects on larger clusters, as discussed in Section 4.

3.2. Shallow impurities in silicon nanocrystals

There is one more type of defect which can play an important role in the optical and transport properties of bulk semiconductors and their low-dimensional counterparts (in particular, silicon). These are impurity centers, of which some experimental results were discussed previously. Let us now consider NCs doped with shallow impurities and discuss impurity states in silicon quantum dots.

Various aspects of the problem have been explored. One of them—the central-cell effect [108–111]—causes splitting of the sixfold degenerate ground energy level in bulk silicon into a singlet, doublet, and triplet with a typical energy splitting of about 10–20 meV for various donors [112]. According to a number of theoretical studies [73, 113–119], in quantum dots doped with donors or acceptors the central-cell potential strengthens the level splitting compared to (i) bulk silicon, and (ii) undoped dots [66, 85, 120, 121]. Investigations of the spatial charge distribution [122, 123], the formation of impurity centers inside silicon nanocrystals from the energy point of view [114–117, 124, 125], intervalley scattering [126], hyperfine splitting and optical gap effects [127], and the screening of the point-charge field [123, 128–136] have been performed. Below, we present EFA calculations of the electronic structure of both donor- and acceptor-doped silicon quantum dots and examine the dependence on the impurity position inside the dot within

the framework of the hydrogenic-impurity model. Also, we discuss the effect of the central-cell potential in screening the point charge in NCs.

3.2.1. Screening in quantum dots

In order to solve accurately the Schrodinger-like equation for the envelope functions in the dot in the presence of an impurity ion, we need the correct expression for the Coulomb potential energy V_C. Its determination in the quantum dot is not a simple task because of the complicated character of screening in NCs. Some authors described the screening properties in an NC with a modified dielectric constant $\varepsilon(R)$ that depends on the dot radius [137–139]. Such a simple model, indeed, gives a moderate increase of the dielectric properties due to the finite size of the crystallite but it does not reflect correctly the local structure of the electric field.

The correct description of such a structure requires first-principles calculations [123, 129–136]. Nevertheless, the microscopic picture permits a clear qualitative macroscopic interpretation using the local dielectric function $\varepsilon(r)$ depending on electron position vector, r. Taking into account the short-range field and charge polarization at the dot boundary due to different static dielectric constants ε_s and ε_d of an NC and its surroundings, one can in principle obtain $\varepsilon(r)$ (Figure 8) [73].

An overall decrease of $\varepsilon(r)$ in a nanocrystal takes place compared to the bulk value of $\varepsilon_s = 12$. As was pointed out earlier [123, 128, 129], this decrease is mainly due to the polarization charges at the dot boundary. The monotonic decrease of $\varepsilon(r)$ extends to the nanocrystal boundary, where the value of the dielectric function becomes equal to ε_d. At the same time, the sharp reduction of $\varepsilon(r)$ toward unity occurring at small r is exclusively due to the short-range central-cell potential.

3.2.2. Donor states in silicon crystallite

First, we consider electronic states in a silicon NC with a hydrogenlike donor placed in some arbitrary position inside the dot. The total electron potential energy described by (2) transforms into $U(\mathbf{r},\mathbf{h}) = U_0(r) + V_C$ where $\mathbf{h}$ stands for the impurity position vector, and V_C is a Coulomb potential energy, including not only the direct electron-ion interaction but also the interaction with polarized charges arising at the dot boundary. Solving the eigenstate and eigenvalue problem for the conduction band [140] yields the ground-state energy splitting shown in Figure 9 at $n_x = 0.8$, $n_y = 0.5$, and $n_z = 0.33$, where $\mathbf{n} = \mathbf{h}/h$, and h stands for the absolute value of $\mathbf{h}$.

In Figure 10, the envelope-function correction $\Delta\Phi$ is shown for the ground state due to the hydrogen-like donor, as a function of the angles θ and φ on the spherical surface $r = h$ for the former values of n_a. Angles θ and φ are the spherical coordinates. The maximal values of $\Delta\Phi$ (light areas in the figure) are located around the donor site marked with the cross. This is a natural result in that the electron density shifts towards the donor site.

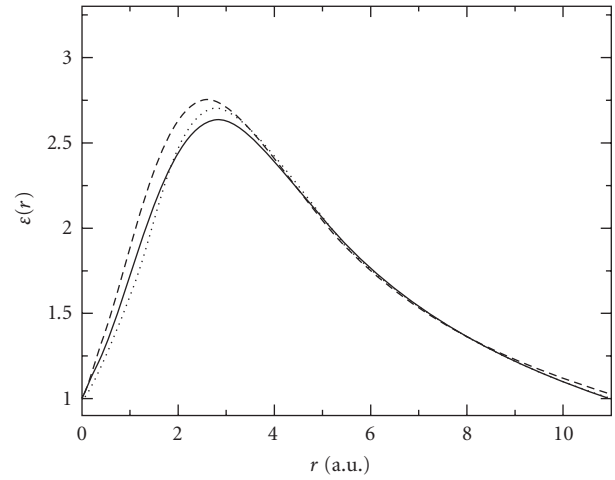

Figure 8: Dielectric function of silicon NCs in silicon dioxide matrix ($\varepsilon_d = 3$) for (1) $R = 1$ nm; (2) $R = 1.75$ nm; (3) $R = 2.5$ nm.

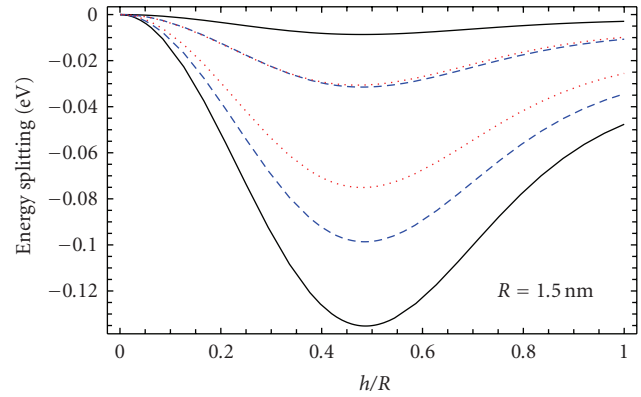

Figure 9: Fine structure of the energy spectrum with respect to the unperturbed sixfold degenerate energy level. Solid lines correspond to two states located in the Brillouin zone at the X-point (001). Dashed line: X-point (010). Dots: X-point (100). The direction of the donor's position vector is defined by $n_x = 0.8$, $n_y = 0.5$, and $n_z = 0.33$. The NC radius is indicated in the figure.

3.2.3. Acceptor states in silicon crystallite

It is interesting to compare the fine structure of the spectrum for donor- and acceptor-doped dots. Obviously, the fine structure in the valence band occurs because of the spin-orbit interaction and the asymmetry of the Coulomb field inside the dot, when the acceptor occupies some noncentral position. The energy splitting has been presented in Figure 11. Similarly to the donor case, the splitting turns out to be large compared to the magnitudes of chemical shifts in bulk silicon [141–144].

The Coulomb and spin-orbit interactions remove the sixfold degeneracy of both lowest levels shown in Figure 5, keeping only the double spin degeneracy of each the levels. Furthermore the splitting increases with decreasing the

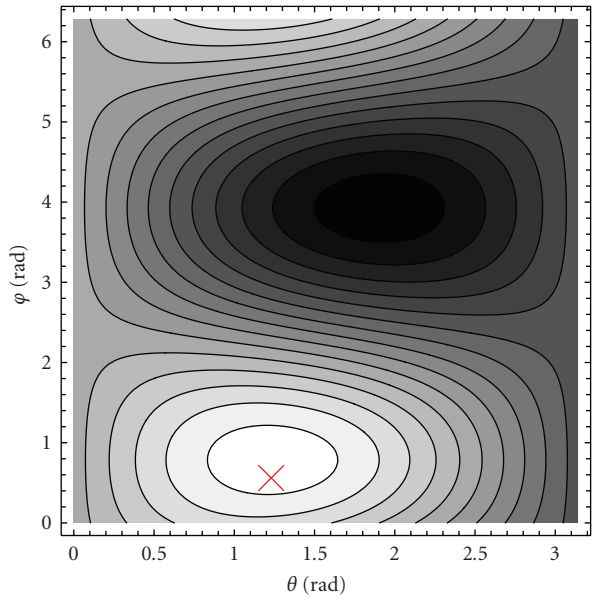

FIGURE 10: Contour plot of the first-order correction to the envelope function for a 3-nm-diameter quantum dot. The value of the correction rises from dark to light. The cross indicates the donor position defined by: $n_x = 0.8$, $n_y = 0.5$, and $n_z = 0.33$. $h/R = 0.46$.

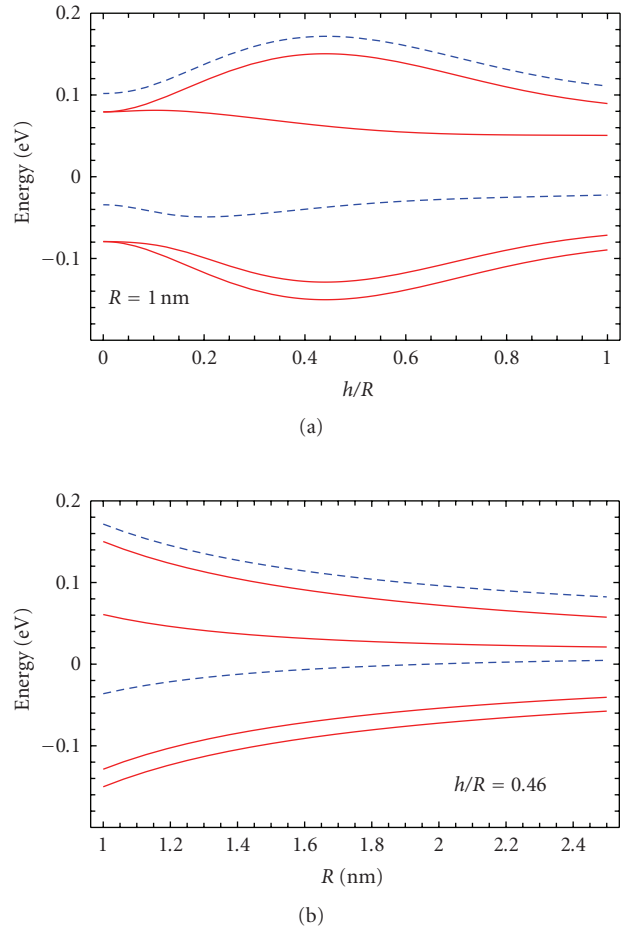

FIGURE 11: Splitting of the two lower hole levels shown in Figure 5 as function of the dimensionless acceptor displacement from the dot center in (a), and with respect to the NC radius in (b). The direction of the acceptor position-vector is defined by $n_x = 0.8$, $n_y = 0.5$, and $n_z = 0.33$. Dashed and solid lines represent the energies originating from doublet and quadruplet at $h = 0$, respectively. All the energies are counted from the mean quadruplet energy at $h = 0$.

nanocrystal size. This is evidence in favor of a quantum confinement effect, as was the case in the donor-doped dots.

The spatial distribution of the hole density in B-doped crystallite for all the six doublets is shown in Figure 12 for $h/R = 0.1$ (upper panels) and $h/R = 0.46$ (lower panels). We have plotted the average of the squared absolute value of the total wave function over the unit cell. In this case the Bloch-function oscillations do not appear in the electron density, which reduces to the "density of envelope function" $\rho_{\text{env}}(\mathbf{r}) = \sum_{j=1}^{6} |\Phi_j(\mathbf{r})|^2$, where $\Phi_j(\mathbf{r})$ is the jth element of the 6D envelope function vector $|\Phi\rangle$ as before.

As the calculations show, for all the six doublets the envelope-function density has an axial symmetry with respect to the line drawn through the NC center and the acceptor. Therefore $\rho_{\text{env}}(\mathbf{r})$ has the same distribution in any dot cross-section to which the acceptor position-vector belongs. Figure 12 shows such a central cross-section of the electron density averaged over the unit cell for all the doublets. Brighter areas in the density plots correspond to higher values of $\rho_{\text{env}}(\mathbf{r})$. The circle represents the nanocrystal boundary, and the bold point situated at the vertical axis indicates the acceptor location.

It should be noted that the general trends in the location of the electron density under the action of the acceptor electric field are, in fact, similar for all the doublets in both cases $h/R = 0.1$ and $h/R = 0.46$. In particular, the ground-state electron density shifts to the acceptor site, while for the excited states, as the energy of the state increases and the electron density gradually moves into the areas free of the acceptor.

3.3. *Interband recombination in silicon nanocrystals*

The PL intensity and quantum efficiency is defined by the relative contribution $\tau_R^{-1}/\tau_{\text{PL}}^{-1}$ of a radiative recombination channel in an interband transition. In turn, the total decay rate is defined by both radiative and nonradiative recombination rates: $1/\tau_{\text{PL}} = 1/\tau_R + 1/\tau_{\text{NR}}$. Consequently, in order to discuss possible means of increasing the quantum efficiency of silicon crystallites, we should understand what factors influence the radiative and nonradiative rates. For this purpose in this section we analyze theoretically both radiative and nonradiative recombination processes.

3.3.1. *Radiative recombination times in undoped Si NCs*

In bulk silicon, no-phonon radiative transitions between the conduction-band Δ-point and the valence-band Γ-point are forbidden because of indirect band-gap of silicon. In

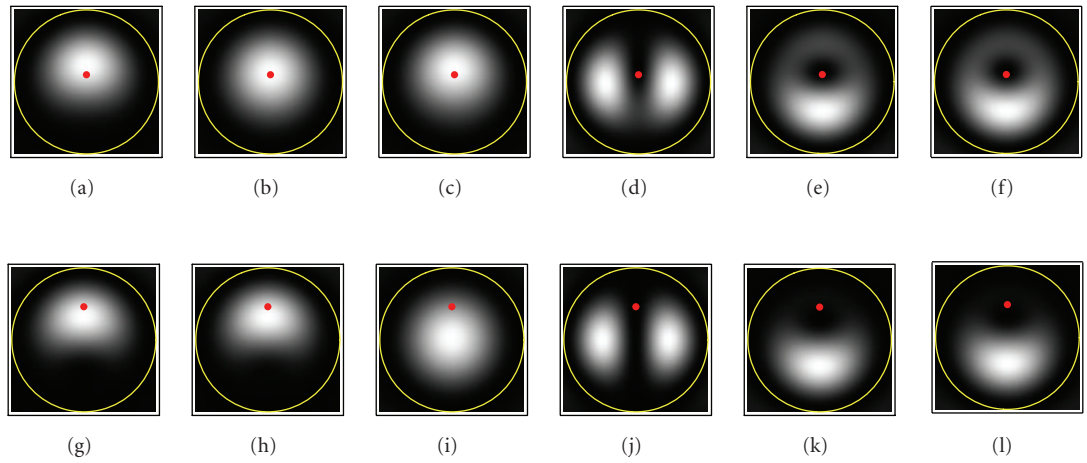

FIGURE 12: Density plot of the probability distribution $\rho_{\text{env}}(\mathbf{r})$ of all the six doublets at $h/R = 0.1$ (upper images), and $h/R = 0.46$ (lower images) for NCs containing a hydrogenic acceptor. The acceptor position is indicated with a red point. (a): ground state; (b) to (f): first to fifth excited states. For each state the hole density is normalized to its maximum in the state, and rises from dark to light. The nanocrystal boundary is marked by the yellow circle, with $R = 1.5$ nm.

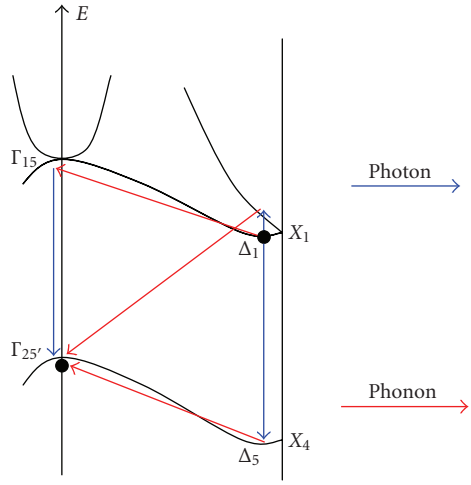

FIGURE 13: Schematic representation of the silicon band structure with phonon-assisted radiative transitions from the conduction-band minimum to the valence-band maximum indicated by arrows.

this case, only phonon-assisted transitions may take place, as shown in Figure 13. In a quantum dot no-phonon emission becomes possible but remains a low probability process for reasons discussed below. Meanwhile, the phonon-assisted radiative transitions have much greater rate. Here, we calculate both no-phonon and phonon-assisted radiative lifetimes in silicon nanocrystal.

We first calculate the rate τ_0^{-1} of the no-phonon radiative recombination. Using Fermi's golden rule in the first-order perturbation theory, one can write the decay rate for the transition between initial (I) and final (F) states in the conduction and valence bands, respectively, in the following form:

$$\tau_{0,IF}^{-1} = \frac{2\pi}{\hbar} \sum_{\mathbf{Q},\sigma} |W_{IF}|^2 \delta(\varepsilon_g(R) - \hbar\omega_\sigma(\mathbf{Q})). \tag{24}$$

Here, $\omega_\sigma(\mathbf{Q})$ and $\mathbf{Q}$ stand for the photon frequency and wave vector. The Dirac delta-function reflects the energy conservation law for the electron transition. The operator W describes the electron-photon interaction, and has the form:

$$W = \sum_{\mathbf{k},\sigma} \sqrt{\frac{2\pi\hbar e^2 \kappa(\varepsilon_s;\varepsilon_d)}{m_0^2 \omega_\sigma(\mathbf{Q}) V_0 \varepsilon_s}} (c_{\mathbf{Q}\sigma} + c_{\mathbf{Q}\sigma}^+) \mathbf{e}_{\mathbf{Q}\sigma} \mathbf{p}, \tag{25}$$

where $\mathbf{p} = -i\hbar\nabla$ is the electron momentum operator, $\mathbf{e}_{\mathbf{Q}\sigma}$ is the polarization vector, the operator $c_{\mathbf{Q}\sigma}$ annihilates and $c_{\mathbf{Q}\sigma}^+$ creates a photon with the wave vector $\mathbf{Q}$ and polarization σ, and V_0 stands for the volume of the electromagnetic resonator. The function $\kappa(\varepsilon_s;\varepsilon_d)$ is written as [145]

$$\kappa(\varepsilon_s;\varepsilon_d) = \sqrt{\frac{\varepsilon_d}{\varepsilon_s}} \left(\frac{3\varepsilon_d}{2\varepsilon_d + \varepsilon_s}\right)^2. \tag{26}$$

This function represents the correction factor in the field magnitude due to the replacement of homogeneous media with bulk permittivity ε_s by a spherical silicon nanocrystal surrounded by silicon dioxide with a dielectric constant ε_d.

The initial state in (24) corresponds to an electron-hole pair being in its ground state, and an ensemble of photons whose distribution over $\mathbf{Q}$ is described by the Bose-Einstein statistics. In the final state, the valence band is completely occupied and the conduction band is empty. The number of photons in the final state always increases by one.

As has already been mentioned (see Section 3.1.2), the ground spinless electron state in the conduction band is sixfold degenerate. However, TB [85, 120], PP [66], and DFT

[121] calculations revealed a weak splitting of the ground state into the singlet, doublet, and triplet states due to the tetrahedral symmetry of the spherical silicon nanocrystal. The authors pointed out that as the NC size varies, A_1-, E-, or T_2-type states alternately become the ground level. Correspondingly, in order to take into account tetrahedral symmetry of the quantum dot, we build the six ground states in accordance with the symmetric transformations of the irreducible representations A_1 (singlet), E (doublet), and T_2 (triplet) of the tetrahedral group. These functions are defined as follows [73]:

$$\begin{aligned}
\Psi_S &= \cos(\lambda)\,|A_1\rangle|s\rangle \\
&\quad + \sin(\lambda)\frac{|X'\rangle|p_x\rangle + |Y'\rangle|p_y\rangle + |Z'\rangle|p_z\rangle}{\sqrt{3}}, \\
\Psi_D^{(1)} &= \cos(\lambda)\,|E^{(1)}\rangle|s\rangle \\
&\quad + \sin(\lambda)\frac{|X'\rangle|p_x\rangle - |Y'\rangle|p_y\rangle}{\sqrt{2}}, \\
\Psi_D^{(2)} &= \cos(\lambda)\,|E^{(2)}\rangle|s\rangle \\
&\quad + \sin(\lambda)\frac{|X'\rangle|p_x\rangle + |Y'\rangle|p_y\rangle - 2|Z'\rangle|p_z\rangle}{\sqrt{6}}, \\
\Psi_T^{(1)} &= \cos(\lambda)\,|X'\rangle|s\rangle \\
&\quad - \sin(\lambda)\frac{\sqrt{2}|A_1\rangle + \sqrt{3}|E^{(1)}\rangle + |E^{(2)}\rangle}{\sqrt{6}}|p_x\rangle, \\
\Psi_T^{(2)} &= \cos(\lambda)\,|Y'\rangle|s\rangle \\
&\quad - \sin(\lambda)\frac{\sqrt{2}|A_1\rangle - \sqrt{3}|E^{(1)}\rangle + |E^{(2)}\rangle}{\sqrt{6}}|p_y\rangle, \\
\Psi_T^{(3)} &= \cos(\lambda)\,|Z'\rangle|s\rangle \\
&\quad - \sin(\lambda)\frac{|A_1\rangle - \sqrt{2}|E^{(2)}\rangle}{\sqrt{3}}|p_z\rangle.
\end{aligned} \tag{27}$$

Here, the parameter λ is defined by the relationships [92]

$$\begin{aligned}
\cos(2\lambda) &= \frac{E_p - E_s - 2H_{pp}}{\sqrt{(E_p - E_s - 2H_{pp})^2 + 4H_{sp}^2}}, \\
\sin(2\lambda) &= \frac{2H_{sp}}{\sqrt{(E_p - E_s - 2H_{pp})^2 + 4H_{sp}^2}},
\end{aligned} \tag{28}$$

where vectors $|s\rangle$ and $|p_a\rangle$ stand for the s- and p-type envelope functions as before. The Bloch states $|A_1\rangle = (|X\rangle + |Y\rangle + |Z\rangle)/\sqrt{3}$, $|E^{(1)}\rangle = (|X\rangle - |Y\rangle)/\sqrt{2}$, $|E^{(2)}\rangle = (|X\rangle + |Y\rangle - 2|Z\rangle)/\sqrt{6}$, and $|T_2\rangle = |X'\rangle$, $|Y'\rangle$, or $|Z'\rangle$ belong to the representations A_1, E, and T_2 of the tetrahedral group. In what follows, when computing the interband matrix elements of W we will choose one of the states given by (27) as the initial one. For convenience, one can rewrite the wave functions of the initial states in a general form:

$$\Psi_I = \sum_{\alpha,j} B_I^{\alpha j} F_\alpha(\mathbf{r})\psi_j(\mathbf{r}), \tag{29}$$

where the index α indicates the "values" of the s, p_x, p_y, and p_z, functions, and $\psi_j(\mathbf{r})$ stands for the six Bloch functions $|X\rangle$, $|Y\rangle$, $|Z\rangle$, $|X'\rangle$, $|Y'\rangle$, $|Z'\rangle$ of the irreducible representation X_1. The s- and p-type envelope functions are denoted as $F(r)$, and $F_x(\mathbf{r})$, $F_y(\mathbf{r})$, $F_z(\mathbf{r})$, respectively. Selecting expansion coefficients $B_I^{\alpha j}$, we can construct any of the states defined by (27).

The final state is one of the three degenerate states (neglecting the spin-orbit coupling) in the valence band [92] with the s-type envelope function:

$$\Psi_F = F(r)\psi_F(\mathbf{r}), \tag{30}$$

where $\psi_F(\mathbf{r})$ stands for the Bloch state basis functions $|YZ\rangle$, $|XZ\rangle$, or $|XY\rangle$ of the irreducible representation $\Gamma_{25'}$.

After some algebra, one can obtain recombination rate $\tau_{0,IF}^{-1}$ in the form:

$$\tau_{0,IF}^{-1} = \frac{4e^2\sqrt{\varepsilon_s}\kappa(\varepsilon_s;\varepsilon_d)\varepsilon_g(R)}{3m_0^2\hbar^2c^3}\,|\mathbf{p}_{IF}|^2, \tag{31}$$

where $\mathbf{p}_{IF} = \langle\Psi_I|\mathbf{p}|\Psi_F\rangle$. In order to compute the momentum matrix element, we expand the Bloch functions $\psi_j(\mathbf{r})$ and $\psi_F(\mathbf{r})$ over the reciprocal lattice vectors $\mathbf{g_n}$ as follows:

$$\begin{aligned}
\psi_j(\mathbf{r}) &= \sum_{\mathbf{m}} C_{j\mathbf{m}} \exp\left[2\pi i(\mathbf{g_m} + \mathbf{e}_j)\mathbf{r}/a_0\right], \\
\psi_F(\mathbf{r}) &= \sum_{\mathbf{n}} V_{F\mathbf{n}} \exp\left[2\pi i\mathbf{g_n}\mathbf{r}/a_0\right],
\end{aligned} \tag{32}$$

where a_0 is the lattice constant of silicon, and unit vectors $\mathbf{e}_j$ define the X-point. We set $\mathbf{e}_{1,4} = \mathbf{e}_x$, $\mathbf{e}_{2,5} = \mathbf{e}_y$, and $\mathbf{e}_{3,6} = \mathbf{e}_z$. Expansion coefficients $C_{j\mathbf{m}}$ and $V_{F\mathbf{n}}$ are determined with the local pseudopotential method. They satisfy the normalizing condition $\sum_{\mathbf{n}}|C_{j\mathbf{n}}|^2 = \sum_{\mathbf{n}}|V_{F\mathbf{n}}|^2 = 1$. As a result, the momentum matrix element is given by

$$\mathbf{p}_{IF} = \frac{\hbar}{4\pi a_0}\mathbf{b}_{IF}(R)\left(\frac{a_0}{R}\right)^4, \tag{33}$$

where $\mathbf{b}_{IF}(R) = \sum_{\alpha,j} B_I^{\alpha j}\mathbf{J}_\alpha(R)$ with $\mathbf{J}_\alpha(R)$ being oscillating vector functions [146] of the dot radius. For s- and p-type subscripts, respectively, these functions are

$$\begin{aligned}
\mathbf{J}(R) &= \sum_{\mathbf{n},\mathbf{m}} \frac{C_{j\mathbf{m}}^* V_{F\mathbf{n}}\mathbf{d}_{\mathbf{n}+\mathbf{m}}}{d_{\mathbf{n}-\mathbf{m}}^4}\cos\left(2\pi d_{\mathbf{n}-\mathbf{m}}\frac{R}{a_0}\right), \\
\mathbf{J}_a(R) &= -i\frac{\sqrt{3}\mu_1}{\pi}\sum_{\mathbf{n},\mathbf{m}} \frac{C_{j\mathbf{m}}^* V_{F\mathbf{n}}\mathbf{d}_{\mathbf{n}+\mathbf{m}}d_{\mathbf{n}-\mathbf{m}}^{(a)}}{d_{\mathbf{n}-\mathbf{m}}^5}\sin\left(2\pi d_{\mathbf{n}-\mathbf{m}}\frac{R}{a_0}\right).
\end{aligned} \tag{34}$$

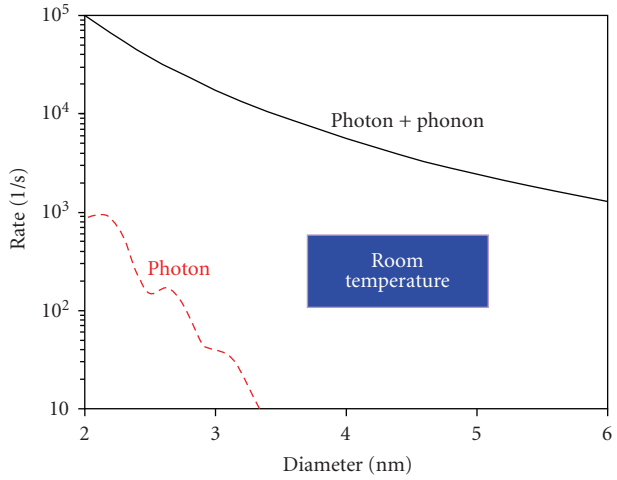

FIGURE 14: Recombination rates of no-phonon and phonon-assisted radiative transitions between the ground electron and hole states in silicon NCs, after averaging over all degenerate initial and final states.

Here, $a = x, y, z$, $\mathbf{d}_{\mathbf{n}\pm\mathbf{m}} = \mathbf{g}_{\mathbf{n}} \pm \mathbf{g}_{\mathbf{m}} \pm \mathbf{e}_j$, and $d^{(a)}_{\mathbf{n}-\mathbf{m}}$ represents an ath component of $\mathbf{d}_{\mathbf{n}-\mathbf{m}}$. The nonzero value of $\mathbf{p}_{IF}$ is exclusively due to the Heisenberg uncertainty relations which cause the wide distribution of the wave function in $\mathbf{p}$-space.

Averaging (31) over all possible initial and final states yields

$$\tau_0^{-1} = \frac{e^2\sqrt{\varepsilon_s}\kappa(\varepsilon_s;\varepsilon_d)\varepsilon_g(R)}{12\pi^2 m_0^2 c^3 a_0^2}\left(\frac{a_0}{R}\right)^8 \left\langle \left|\mathbf{b}_{IF}(R)\right|^2\right\rangle. \tag{35}$$

In Figure 14 we show the no-phonon recombination rate τ_0^{-1} as function of the dot size. Although the no-phonon decay rate has a nonzero value, its magnitude remains small (less than $10^3\ \mathrm{s}^{-1}$) within the range of the NC sizes shown in the figure.

Next, we calculate the phonon-assisted recombination rate [95, 147–149]. The total phonon-assisted rate of the radiative electron-hole recombination is determined in the second-order perturbation theory as

$$\begin{aligned}\tau_{R,IF}^{-1} = {} & \frac{2\pi}{\hbar}\sum_{\mathbf{Q},\sigma}\sum_{\mathbf{q},\ell}\left|\sum_a \frac{W_{FA}U_{AI} + U_{FA}W_{AI}}{\varepsilon_I - \varepsilon_A}\right|^2 \\ & \times\left[\delta(\varepsilon_g(R) - \hbar\omega_\sigma(\mathbf{Q}) - \hbar\nu_\ell(\mathbf{q})) \right. \\ & \left. + \delta(\varepsilon_g(R) - \hbar\omega_\sigma(\mathbf{Q}) + \hbar\nu_\ell(\mathbf{q}))\right].\end{aligned} \tag{36}$$

Here the matrix elements of the electron-photon (W) and electron-phonon (U) interaction operators are calculated between the initial I, the final F, and an intermediate state A; ε_A and ε_I are the total energies of the intermediate and initial states, respectively, including not only the energies of the electrons (or holes) but also the energies of the photons and phonons. The phonon frequency of ℓth polarization is denoted as $\nu_\ell(\mathbf{q})$ with $\mathbf{q}$ being the dimensionless phonon wave vector taken in units of $2\pi/a_0$.

The electron-phonon interaction operator is treated within the framework of the rigid-ion model and is given by

$$\begin{aligned}U = {} & -\sum_{\mathbf{q},\ell}\sum_{\mathbf{n},s}\sqrt{\frac{\hbar}{2MN\nu_\ell(\mathbf{q})}}\nabla V_{\mathbf{n}s} \\ & \times\left(\mathbf{e}_{\mathbf{q}\ell s}\exp\left\{\frac{i2\pi\mathbf{q}\mathbf{R}_{\mathbf{n}}}{a_0}\right\}b_{\mathbf{q}\ell}\right. \\ & \left. + \mathbf{e}^*_{\mathbf{q}\ell s}\exp\left\{-\frac{i2\pi\mathbf{q}\mathbf{R}_{\mathbf{n}}}{a_0}\right\}b^+_{\mathbf{q}\ell}\right).\end{aligned} \tag{37}$$

Here, N is the number of primitive cells in the crystal, M is the mass of a silicon atom, $V_{\mathbf{n}s} = V_{\mathrm{at}}(\mathbf{r}-\mathbf{R}_{\mathbf{n}}-\boldsymbol{\tau}_s)$ is the atomic potential, where $\mathbf{R}_{\mathbf{n}}$ stands for the position vector of the $\mathbf{n}$th unit cell, and $\boldsymbol{\tau}_s$ represents the position vectors of two atoms within the unit cell: $\boldsymbol{\tau}_1 = 0$, and $\boldsymbol{\tau}_2 = (1,1,1)\times a_0/4$, $b^+_{\mathbf{q}\ell}$ and $b_{\mathbf{q}\ell}$ are the phonon creation and annihilation operators, and the phonon polarization vectors are denoted as $\mathbf{e}_{\mathbf{q}\ell s}$. Making the Fourier transformation of the atomic potential: $V_{\mathrm{at}}(\mathbf{r}) = N^{-1}\sum_{\mathbf{p}} V_{\mathbf{p}}\exp\{i\mathbf{p}\mathbf{r}\}$, one can rewrite the operator U in the form (see also [150, 151]):

$$\begin{aligned}U = {} & \frac{2\pi i}{a_0}\sum_{\mathbf{q},\ell,s,\mathbf{m}}\sqrt{\frac{\hbar}{2MN\nu_\ell(\mathbf{q})}}(\mathbf{q}+\mathbf{g}_{\mathbf{m}}) \\ & \times\left[\mathbf{e}^*_{\mathbf{q}\ell s}V^*_{\mathbf{q}+\mathbf{g}_{\mathbf{m}}}\exp\left\{-\frac{i2\pi(\mathbf{q}+\mathbf{g}_{\mathbf{m}})(\mathbf{r}-\boldsymbol{\tau}_s)}{a_0}\right\}b^+_{\mathbf{q}\ell}\right. \\ & \left. - \mathbf{e}_{\mathbf{q}\ell s}V_{\mathbf{q}+\mathbf{g}_{\mathbf{m}}}\exp\left\{\frac{i2\pi(\mathbf{q}+\mathbf{g}_{\mathbf{m}})(\mathbf{r}-\boldsymbol{\tau}_s)}{a_0}\right\}b_{\mathbf{q}\ell}\right].\end{aligned} \tag{38}$$

Calculations of the electron-photon and electron-phonon matrix elements yield

$$\begin{aligned}\tau_{R,IF}^{-1} = {} & \frac{4\pi^2\hbar^2e^2\sqrt{\varepsilon_s}\kappa(\varepsilon_s;\varepsilon_d)\varepsilon_g(R)}{3Mm_0^2c^3a_0^4}\left(\frac{a_0}{R}\right)^3 \\ & \times\sum_\ell\frac{P_{IF}(\ell)}{\hbar\nu_\ell}\coth\left[\frac{\hbar\nu_\ell}{2kT}\right],\end{aligned} \tag{39}$$

where

$$\begin{aligned}P_{IF}(\ell) = {} & B_I^{\alpha m}\left(B_I^{\beta n}\right)^* x_{Fm}(\ell)x_{Fn}(\ell)2\pi^2R^3 \\ & \times\int d\mathbf{r}F_\alpha(\mathbf{r})F_\beta(\mathbf{r})F^2(r), \\ x_{Fm}(\ell) = {} & \sum_A\frac{\langle\psi_F|w|\psi_A\rangle\langle\psi_A|u|\psi_m\rangle + \langle\psi_F|u|\psi_A\rangle\langle\psi_A|w|\psi_m\rangle}{\varepsilon_I - \varepsilon_A}.\end{aligned} \tag{40}$$

ψ_A represents the Bloch functions of the intermediate states and the operators w and u are directly proportional to W and U:

$$\begin{aligned}W = {} & w\frac{2\pi\hbar}{a_0}\sqrt{\frac{2\pi\hbar e^2\kappa(\varepsilon_s;\varepsilon_d)}{m_0^2\omega(\mathbf{Q})V_0\varepsilon_s}}, \\ U = {} & u\frac{2\pi}{a_0}\sqrt{\frac{\hbar}{2MN\nu_\ell(\mathbf{q})}}.\end{aligned} \tag{41}$$

As has been shown earlier, the electron subsystem in silicon nanocrystals interacts more efficiently with TO and LO phonons [147, 148] similarly to bulk silicon [150, 151]. The contribution of TA phonons is negligibly small. Therefore, in the sum over the phonon modes in (39), only TO and LO modes may be taken into account.

For convenience, we have again averaged the calculated rates over all the possible initial and final degenerate states and obtained the recombination rate in the following form:

$$\tau_R^{-1} = \frac{\pi^2\hbar^2 e^2 \varepsilon_g(R)\sqrt{\varepsilon_s}\kappa(\varepsilon_s,\varepsilon_d)}{9Mm_0^2c^3a^4}\left(\frac{a_0}{R}\right)^3 \times \left(\frac{7.527\coth\left[\hbar\nu_{\mathrm{LO}}/2kT\right]}{\hbar\nu_{\mathrm{LO}}} + \frac{32.768\coth\left[\hbar\nu_{\mathrm{TO}}/2kT\right]}{\hbar\nu_{\mathrm{TO}}}\right) \times (4\cos^2\lambda + 9.26). \tag{42}$$

Here: $\hbar\nu_{\mathrm{LO}} = 0.051$ eV and $\hbar\nu_{\mathrm{TO}} = 0.0576$ eV represent the energies of LO and TO phonons and the numbers 7.527, 32.768 come from numerical integration of electron-phonon matrix elements. The size dependence of the recombination rate has been presented in Figure 14. The dependence of τ_R^{-1} on the dot radius is close to R^{-3}. This is much slower than the rate obtained for no-phonon transitions (R^{-8}).

The results presented here agree well both qualitatively and quantitatively with those obtained by other authors [95, 147, 148] for similar systems. In particular, according to their results, the recombination rates for NCs from 2 to 6 nm in diameter do not exceed $10^5\,\mathrm{s}^{-1}$ and are never less than $5 \times 10^2\,\mathrm{s}^{-1}$. It should be noted, however, that the TB calculations [148] produce a considerably slower decrease of the radiative decay rate than the EFA (as developed here and in [95, 147, 149]) predicts.

Finally, concluding this subsection, we would like to discuss briefly the relation between our single-particle calculations and the singlet-triplet model which gives a reduction of the radiative lifetime with increasing temperature, as in (1). It is, of course, not applicable in the frame of a single-particle treatment to obtain the state splitting caused by the exchange electron-hole interaction. Therefore, the temperature dependence of τ_R^{-1} (42) is defined exclusively by the phonons. As a result, no sharp rise of the decay rate appears in our model as the temperature increases up to the room values. At temperatures higher than about 150–200 K, both models nevertheless should give similar results because the upper excitonic states become highly populated. Thus, the single-particle model remains valid for $T > 200$ K. As well, it should be noted that the separation of dark and bright excitons is not always possible. The spin-orbit coupling transforms forbidden exciton transitions into suppressed ones due to the entanglement of single-particle states with different spin projections. The entanglement can be crucially strengthened by imperfections of the crystallite structure such as shape nonsphericity or, especially, by various point defects such as P_b centers, SiO bonds, and impurities. In the presence of the latter effects, all the transitions can become allowed and consequently the single-particle model is acceptable.

3.3.2. Radiative recombination in doped dots

Experimental evidence of shallow impurity effects in the PL of silicon NCs (see Section 2.3) has no corresponding rigorous theoretical grounds. Usually, when discussing various changes in optical properties of the NCs due to doping, the nonradiative recombination channel is considered more closely. For instance, doping may passivate dangling bonds, and, as a consequence, essentially reduce the effectiveness of the nonradiative channel. On the other hand, a large number of donors or acceptors in the nanocrystal leads to the appearance of extra carriers that can recombine through the Auger process. Thus, doping is an important factor influencing the nonradiative recombination (a more detailed description of the nonradiative recombination mechanisms can be found in the next subsection). The nonradiative lifetime τ_{NR} can be varied by doping, which leads to the change of the emission efficiency.

The impact of doping on the radiative channel has not yet reported. However, it is interesting to examine also the possibility of increasing the quantum yield via enhancement of the radiative rate τ_R^{-1}. This is exclusively a quantum effect that can be explained by the reconstruction of the wave functions in different symmetry (or asymmetry), and changing selection rules for the interband transitions. We would like to touch upon this question in the present subsection and compute the radiative recombination rates in a silicon NC doped with a hydrogen-like donor and acceptor.

In order to compute the decay rates for the doped dot we follow (36). The main reason for the rate changes compared to the case of the undoped dot lies in some corrections to the electronic wave functions of both initial and final states (27), (30) due to the existence of a shallow impurity in the dot. In the following, we discuss two different cases.

The first case corresponds to an off-center position for the impurity inside the dot. In the valence band such an impurity location creates a field asymmetry in the system, which entangles the three spinless s-type states (30) with the three spinless p-type states [92]

$$\begin{aligned}\Psi_{p1} &= \frac{F_x(\mathbf{r})|XZ\rangle - F_y(\mathbf{r})|YZ\rangle}{\sqrt{2}},\\ \Psi_{p2} &= \frac{F_z(\mathbf{r})|YZ\rangle - F_x(\mathbf{r})|XY\rangle}{\sqrt{2}},\\ \Psi_{p3} &= \frac{F_y(\mathbf{r})|XY\rangle - F_z(\mathbf{r})|XZ\rangle}{\sqrt{2}}.\end{aligned} \tag{43}$$

These states (30) and (43) correspond to the closely spaced lowest triply degenerate energy levels shown in Figure 5. As a result, the ground hole state becomes a superposition of the states with s- and p-type envelope functions. In the conduction band, the ground electron states are the s-p combinations even without impurities, as seen from (27). Embedding the impurity into some arbitrary position within the NC raises the number of the p-type envelope functions in the ground states as well as in the valence band. However, $P_{IF}(\ell)$ becomes smaller if the integrated envelope functions are p-type. Consequently, the squared transition matrix element, proportional to $P_{IF}(\ell)$, and the rate itself decrease

relative to the case of an undoped NC, as shown in Figure 15 for two different displacements of the impurity from the dot center.

The ratio $h/R = 0.46$ corresponds to the greatest possible mix of s- and p-type states with maximal weight of the p-type envelope functions in the ground states both in the conduction and valence bands. The strong mixing results in maximal decrease of the decay rate independently of the impurity type. When the impurity is situated near the nanocrystal boundary, $h/R = 0.9$, the weight of the p-type envelope functions reduces in the ground state of both bands. As a consequence, the rate rises with respect to the case $h/R = 0.46$, but remains smaller than that for the undoped NC.

The second case we consider is the case of the central-located impurity. If $h = 0$, no s-p entanglement takes place in the valence band. The functions with the s-type envelope (30) describe the ground states of both donor- and acceptor-doped NCs.

The situation is different for the conduction band. Formally, the wave functions of the six spinless ground states are described by (27) as before. However, for doped dots, parameter λ has a form which differs from that given by (28). In the presence of an impurity center, λ is defined as:

$$\cos(2\lambda) = \frac{E_p - E_s + \delta V - 2H_{pp}}{\sqrt{\left(E_p - E_s + \delta V - 2H_{pp}\right)^2 + 4H_{sp}^2}},$$
$$\sin(2\lambda) = \frac{2H_{sp}}{\sqrt{\left(E_p - E_s + \delta V - 2H_{pp}\right)^2 + 4H_{sp}^2}}, \quad (44)$$

where $\delta V = V_{pp} - V_{ss}$ is the difference between the p-p and s-s type matrix elements of the Coulomb potential energy V_C. The appearance of this term in the definition of λ is explained by the shift of the energy levels of the s- and p-states E_s and E_p, respectively, due to the Coulomb interaction. The relative shift δV turns out to be positive for donors, and negative for acceptors. Consequently, $\cos(\lambda)$ increases and $\sin(\lambda)$ decreases for donors, and vice versa for acceptors.

This implies that the weight of the s-type envelope function in the electron ground state increases for the donor-doped dot and shrinks for the dot doped with acceptor, with respect to its value in the undoped dot. Hence, the coefficient $P_{IF}(\ell)$ for the donor-doped dot is greater than that for the undoped dot. In turn, the latter exceeds $P_{IF}(\ell)$ for the acceptor-doped dot. Precisely the same relationships take place for the recombination rates, as shown in Figure 15.

Note in conclusion, that the central-symmetric case $h = 0$ qualitatively corresponds to some real situation, where the NC has been highly doped with donors or acceptors. It is natural to assume a homogeneous impurity distribution within the nanocrystal in this case. Obviously, such a homogeneous density of charge induces a spherically symmetric electric field that cannot mix the s- and p-type states. Moreover, the relative Coulomb shift δV remains positive for donors and negative for acceptors, as in the above case of a single impurity center in the dot [73]. Therefore, one can expect similar behavior of τ_R^{-1} for highly doped NCs.

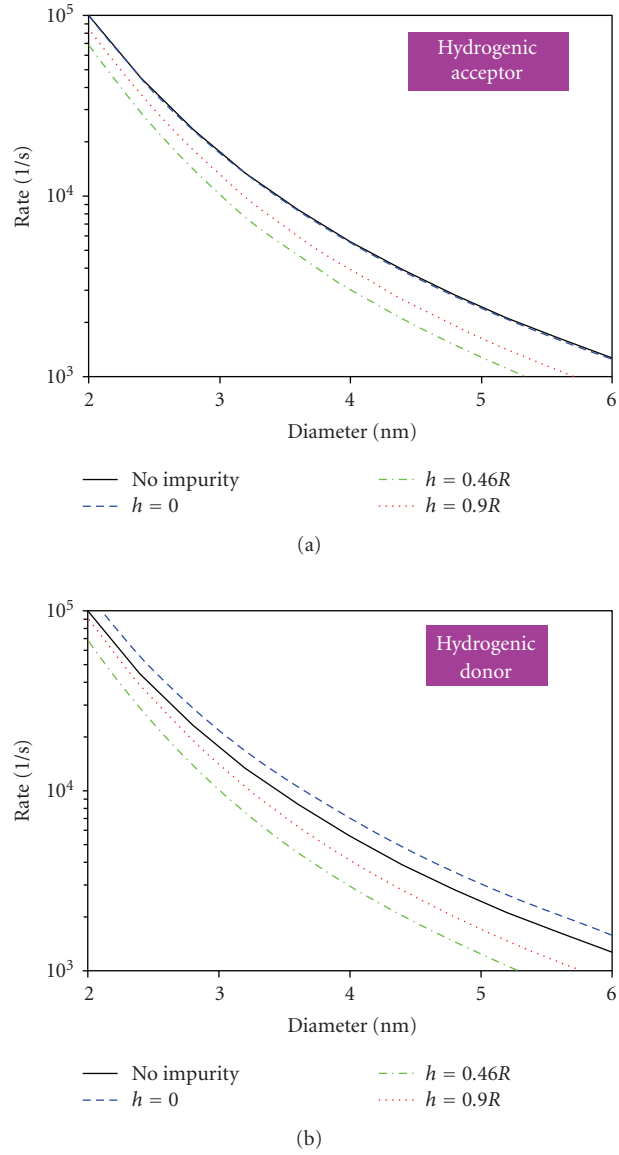

Figure 15: The rates of the phonon-assisted ground radiative transition as functions of the dot radius for a doped dot. For $h \neq 0$, we have $n_x = 0.8$, $n_y = 0.5$, and $n_z = 0.33$.

3.3.3. Nonradiative recombination

In parallel with radiative transitions, nonradiative processes occur in silicon nanocrystals. As a rule, nonradiative processes play a problematic role in silicon crystallites, due to their high recombination rates which substantially exceed the rates of the radiative transitions. Among the possible nonradiative processes, capture on dangling bonds and Auger recombination are the most efficient. Both processes are phonon-assisted, possibly even multi-phonon. The first one takes place both at low and high pumping levels, while Auger recombination becomes possible exclusively at high excitation power when more than one excited electron (hole) exist in the conduction (valence) band of the nanocrystal.

The capture on a neutral dangling bond has been studied earlier by TB method [100, 106]. It was shown that excited electron-hole pairs can recombine on a neutral dangling bond in two stages. First, the electron (hole) is trapped on a neutral P_b center making it negatively (positively) charged. Then, the hole (electron) is trapped on the charged dangling bond. According to estimations [100], the capture rate on the neutral dangling bond for holes is always much greater than that for electrons. In turn, the electron capture rate at room temperature increases sharply as the nanocrystal gap decreases from 2.7 eV to 1.5 eV (see (23)). Within the same range of energy gaps, the hole capture rate also increases but less sharply. We should emphasize the presence of two main features of the capture process. First, there is a very stron dependence of the capture rates (even for holes) on the energy gap, that is, the NC size. The second feature is the overall high capture rates, which are much greater than the radiative decay rates. Evidently, the presence of a dangling bond in silicon crystallite drastically reduces the quantum efficiency of photon generation. Therefore the passivation of dangling bonds is required for achievement of relatively efficient luminescence.

Let us now touch briefly on the role of SiO defects in the photoluminescence. The calculations of Nishida [102] showed that the oscillator strength is almost independent of the existence of Si–O–Si bonds. In contrast, the Si=O bonds reduce the oscillator strength by several orders of magnitude. Recently, however, Sa'ar et al. [64] demonstrated experimentally that both back-bonded and double-bonded oxygen atoms can enhance the PL intensity due to formation of coupled states of electrons (holes) and SiO vibrations. Such vibrations induce electric polarization fields generating long-lived coupled states named "vibrons". Usually, the surface vibrations scatter the carriers; however, vibrons, being coupled states, do not scatter the carriers and thereby exclude one of possible nonradiative channels from the recombination process.

For highly excited nanocrystals, Auger recombination may take place. It is sufficient to have only three particles (two electrons and a hole, or vice versa) for this process to occur. It is well known that Auger recombination has high efficiency in bulk silicon. Therefore, it is natural to expect a similar behavior in silicon crystallites. Calculations of the Auger-recombination rate in crystallites carried out with TB [58, 152] and EFA [153] techniques confirm, indeed, the fast character of this mechanism. In particular, the characteristic times have been found to be of the order 0.1 to 10 ns^{-1} and gradually rise with decreasing nanocrystal size. Thus, Auger recombination, as well as dangling bonds, can strongly quench the luminescence in silicon crystallites, as confirmed experimentally [152].

4. ENSEMBLES OF QUANTUM DOTS

4.1. Size distributions

As discussed in detail in the previous sections, the recombination energy for Si NCs is dependent on the NC size. In order to achieve optical gain and stimulated emission, therefore, a narrow size distribution would be beneficial in order to narrow the gain profile. In ensembles of silicon nanocrystals grown by various thin film methods or by ion implantation, it is so far not possible to obtain the narrow size distributions that can be achieved with chemical methods, where post-synthesis size selection methods are routinely employed [154]. However, there is hope for better size selectivity, as will be discussed toward the end of this section.

The nucleation and growth behavior of nanocrystals in ion implanted systems, in particular, has been extensively characterized [155, 156]. The lognormal size distribution results in general when multiple microscopic processes govern the nucleation and growth kinetics, as is typical in these systems. The lognormal distribution is found even in cases where the "memory" of the specific initial conditions is lost, for example, after annealing of ion implanted samples [156]. In such cases, the nanocrystal size distribution is governed by the standard lognormal curve:

$$P(x) = \frac{1}{Sx\sqrt{2\pi}} \exp\left[\frac{-(\ln(x) - M)^2}{2S^2}\right], \tag{45}$$

where the mean and variance can be related to the M and S parameters by $\mu = \exp(M + S^2/2)$ and $\text{var} = \exp(S^2 + 2M)[\exp(S^2) - 1]$.

For thin films also, a lognormal distribution is predicted on the basis of random nucleation and growth in a homogeneous medium, regardless of the growth temperature, specific method of crystallization, and the mean grain size [157, 158], which is consistent with previous theories on cluster growth in metals and ceramics [159]. Lognormal distributions in the case of silicon grains crystallizing in amorphous silicon have been reported [157], and the lognormal size distribution has also been observed in silicon NCs over the range of annealing temperatures from 400 to 1100°C [47, 160]. Figure 16 shows the size distributions obtained from TEM data for two samples available in the literature. In Figure 16(a), the data from Vinciguerra et al. [161] are reproduced along with a Gaussian least squares fit ($\mu_{\text{radius}} = 1.68\,\text{nm}$, $\sigma = 0.65\,\text{nm}$) which is similar to the fit in the original publication (quoted as $\mu = 1.7 \pm 0.6\,\text{nm}$), and a lognormal fit with $S = 0.27$ and $M = 0.54$). The data *look* decidedly lognormal with a skew toward large radii; the lognormal fitting matches the data better on both the high and low tails of the distribution, has a better correlation ($R^2 = 0.94$ versus 0.86), and is naturally equal to zero for negative radii. Figure 16(b) shows the original data from Glover and Meldrum [162], along with a lognormal fit with $S = 0.29$, $M = 0.22$. This latter data and fit will be used in the model in the following subsections. Obviously, the exact numbers obtained for M and S depend on the histogram binning and on the quantity of the data.

Size distributions can potentially be different than lognormal whenever the nucleation and growth processes are not random but are controlled in some way, such as via irradiation-induced nucleation [163], or through nonuniformities in the concentration of silicon, or when size selection is built into in the process as, for example, in the formation

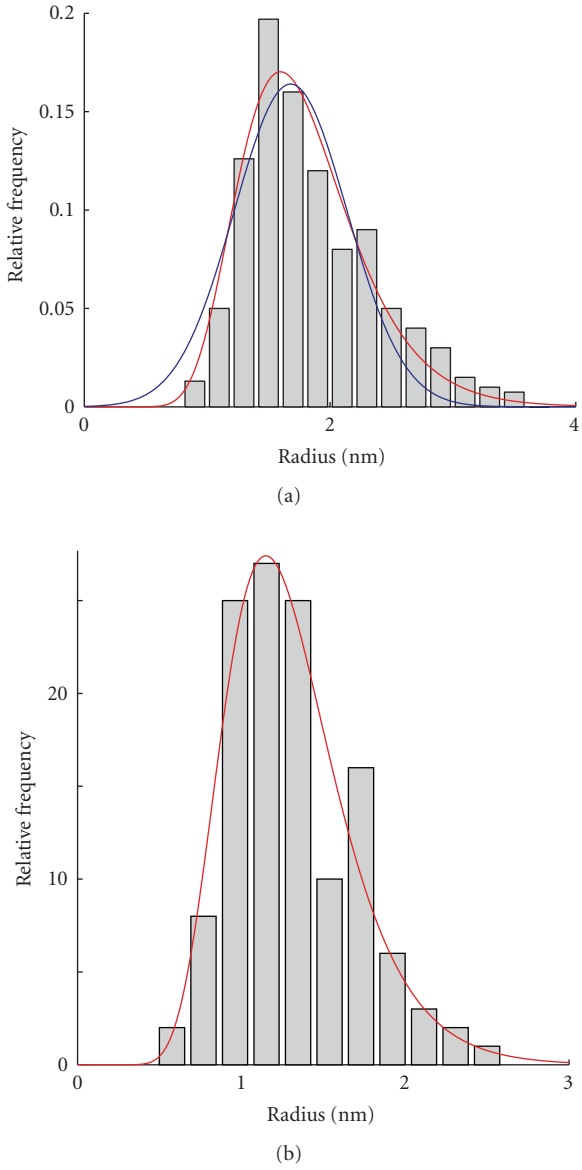

FIGURE 16: (a) Experimental size histogram from [161], with a Gaussian fit (blue line) and a lognormal fit (red line). Panel (b) shows the data from [162] with a lognormal fit.

of silicon nanocrystals by laser pyrolysis [164], or when size selection is done after crystal formation in solution, or when there is a mechanism for producing nonuniform (i.e., bimodal) distributions. Nevertheless, in numerous studies of silicon nanocrystals a Gaussian distribution is assumed. It can be mentioned that in most cases where a Gaussian fit is used to model the silicon NC size distribution, there is in fact no theoretical basis for it. In fact, it can predict unphysical results (e.g., the Gaussian function does not go to zero when its argument—the radius or diameter—is negative).

The lognormal function should, therefore, be used in cases except those in which there are reasons to expect a different distribution. Since there is a strong dependence of the bandgap energy on the cluster size, accurate modeling of the behavior of ensembles of Si NCs does imply that the size distributions should be well known and correctly modeled. For modeling luminescent properties of ensembles of silicon nanocrystals, as discussed below, the lognormal distribution will be used in every case.

4.2. PL spectra and dynamics

Silicon NCs are characterized by a broad emission spectrum typically peaked between 800 and 900 nm, with a full-width-at-half-maximum (FWHM) of as much as 200 nm, even in "monodispersed" multilayered samples [165]. Although the size distributions for the monodispersed samples in [165] were not actually reported, it seems likely that they would nevertheless be much wider than typically obtained for CdSe NCs due to the lack of post-synthesis size selection methods. Therefore, the broad emission band could simply be due to the range of confined carrier energies in clusters of different sizes, or to the random nature of the interface states that may affect the PL spectrum. Single quantum dots may show homogeneous broadening up to ~150 meV at room temperature [19], although this is still narrower than the overall inhomogeneous broadening due to the size distribution. Below, we will investigate the spectral effects of broadening and nonradiative defects on the emission spectrum of an ensemble of Si NCs.

In order to investigate the theoretical luminescence spectrum and dynamics, the NC size distribution for SiO films annealed at 1000°C from [47] (lognormal radius parameters $S = 0.21$, $M = 0.74$) was used along with the theory developed in Sections 1–3. First, the effect of inhomogeneous broadening was investigated by plotting one spectrum in which the energies of 10^6 NCs produced with a lognormal probability function were binned in histogram form. In this case, for simplicity the NCs were treated as isolated, and energy transfer between them was not permitted (purple curve, Figure 17). The effect of homogeneous broadening was determined by assigning each cluster a Gaussian range of emission energies with standard deviations ranging from 0 to 200 meV and adding all the resulting curves (Figure 17). As the homogeneous broadening increases, the emission spectrum became broader, effectively similar to a "Gaussian smoothening" of the spectrum. Additionally, the spectrum was observably wider even for small levels of homogeneous broadening, and the peak shifts to slightly shorter wavelengths due to the overall shape of the lognormal function. The spectrum maximizes at shorter wavelengths than actually observed for a real specimen with this size distribution because NC-NC interactions were not yet turned on in the simulation. At this stage, the intent is simply to demonstrate the effect of homogeneous broadening on the observed PL spectrum. One may furthermore propose that the term "monodisperse" may only be used rigorously in situations in which the width of the PL spectra is governed primarily by homogeneous rather than inhomogeneous spectral broadening.

Next, the effect of nonradiative interface defects on the emission spectra and dynamics was estimated. Two size

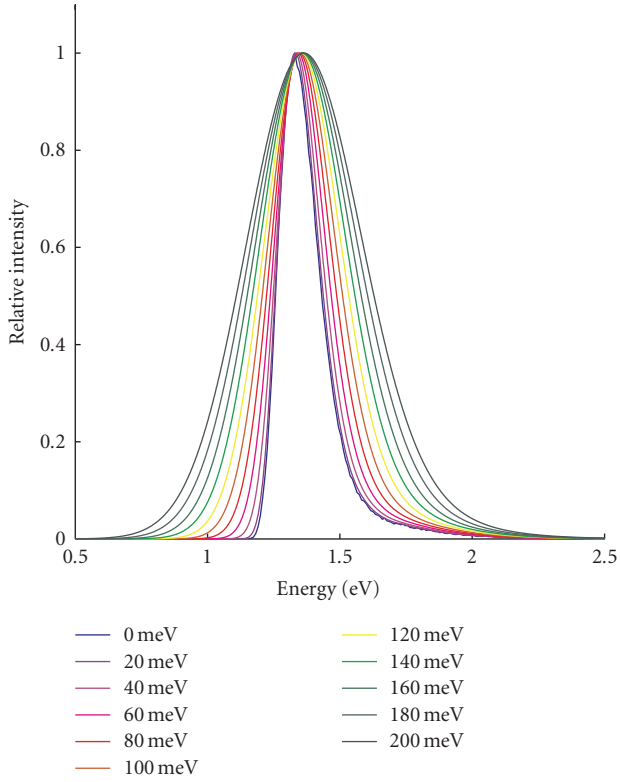

Figure 17: Effect of homogeneous broadening on the simulated (normalized) PL spectrum. The FWHM of the Gaussian homogeneous broadening is shown in the legend.

distributions corresponding to those in [47] ($S = 0.21$; $M = 0.74$) and [162] ($S = 0.29$; $M = 0.22$) were used, and for the present evaluation NC-NC energy transfer was not permitted. Several different concentrations of nonradiative defects ranging from 0 to $10^{20}\,\mathrm{cm}^{-3}$ were assigned to the clusters with probabilities weighted proportionally to the surface areas. Clusters were checked in random order and a defect was assigned to a cluster if the random number was smaller than $A_{\mathrm{NC}}/A_{\mathrm{all\,NCs}}$. The process was continued until all defects had been assigned, allowing for multiple defects on a single particle (Figure 18). Every cluster was then given an electron-hole pair with a lowest excited-state energy calculated according to (22). The radiative and nonradiative rates were calculated from (42) and (23), respectively. Using a simple Monte Carlo procedure, the probabilities of radiative and nonradiative decay were calculated for each NC and a random number generator used to determine whether either type of decay occurred. This process continued until no excited carriers remained.

The resulting PL spectra were characterized by an asymmetric curve shape, tailing toward higher energies due to the form of the equations leading up to (22) (Figure 19). The effect of various concentrations of nonradiative surface defects is clearly observable in the simulated PL spectra. In addition to decreasing the overall PL intensity, the effect of the nonradiative centers is to blueshift the peak wavelength. The spectral blueshift occurs because the larger

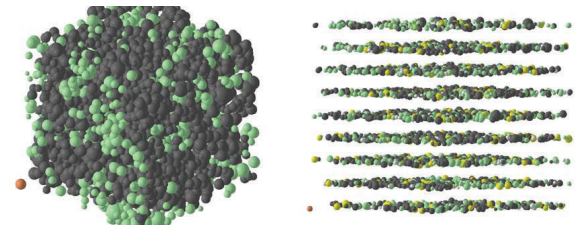

Figure 18: Left: Plot of a simulation box, 4000 NCs, initial state. Dark clusters contain one or more defects. Right: multilayered sample in a time window between 50–100 μs after the end of the pump pulse. Yellow NCs had a radiative recombination event during this time period and white NCs have no charge carriers remaining. Interaction effects were turned off for these simulations. The orange NC in the lower left corner of both images is 5 nm in diameter.

clusters are statistically more likely to contain defects, and the effect would be even stronger if defects were assigned with a volume rather than surface-area weighting (e.g., for volume defects). If extended annealing periods can remove nonradiative centers without increasing the NC size [166], then the effect would be to cause an increased intensity and a redshift of the PL peak, exactly as reported experimentally [53]. This redshift is not due to increasing cluster size, but is due to the removal of nonradiative traps. Finally, the high-energy skewness of the simulated spectra is due to a combination of effects, including the lognormal size distribution, and the lack of carrier transfer from small to large clusters.

As discussed in Section 1, PL decay dynamics in ensembles of Si NCs are characterized by the "stretched exponential" function $I_t/I_0 = \exp[-(t/\tau)^{\beta}]$, with values of the exponent β often between 0.7-0.8. The stretched exponential has been suggested to be due to a hopping mechanism in which excitons are temporarily trapped and delayed at sites in the oxide matrix or at the cluster-oxide interfaces [32, 167, 168]. However, the stretched exponential decay could also be due to the distribution of lifetimes in NCs of different sizes, as has been indicated by a few groups [35, 169]. In the absence of radiative centers, the recombination energy is given by (22), and the size-dependent radiative rates were developed in (42). Here we found that when the defect concentration was set to zero (uppermost line in Figure 20), values of $\beta = 0.58$ and $\tau = 33\,\mu$s emerged naturally. The small lifetime is due to the small size of the clusters used in this simulation. Also, since interactions were not enabled, there is no energy transfer from small to large clusters which would also affect the time constant (and the value of β). Including defects changed these values considerably: with increasing defect concentration, the decays are more precipitous (Figure 20). The stretched exponential function with low β values can, therefore, be obtained naturally as a result of the lifetime distribution. Approximately 100-microsecond-timescale carrier hopping, as suggested in previous work [168] as an explanation for the stretched exponential decay, while not ruled out by this

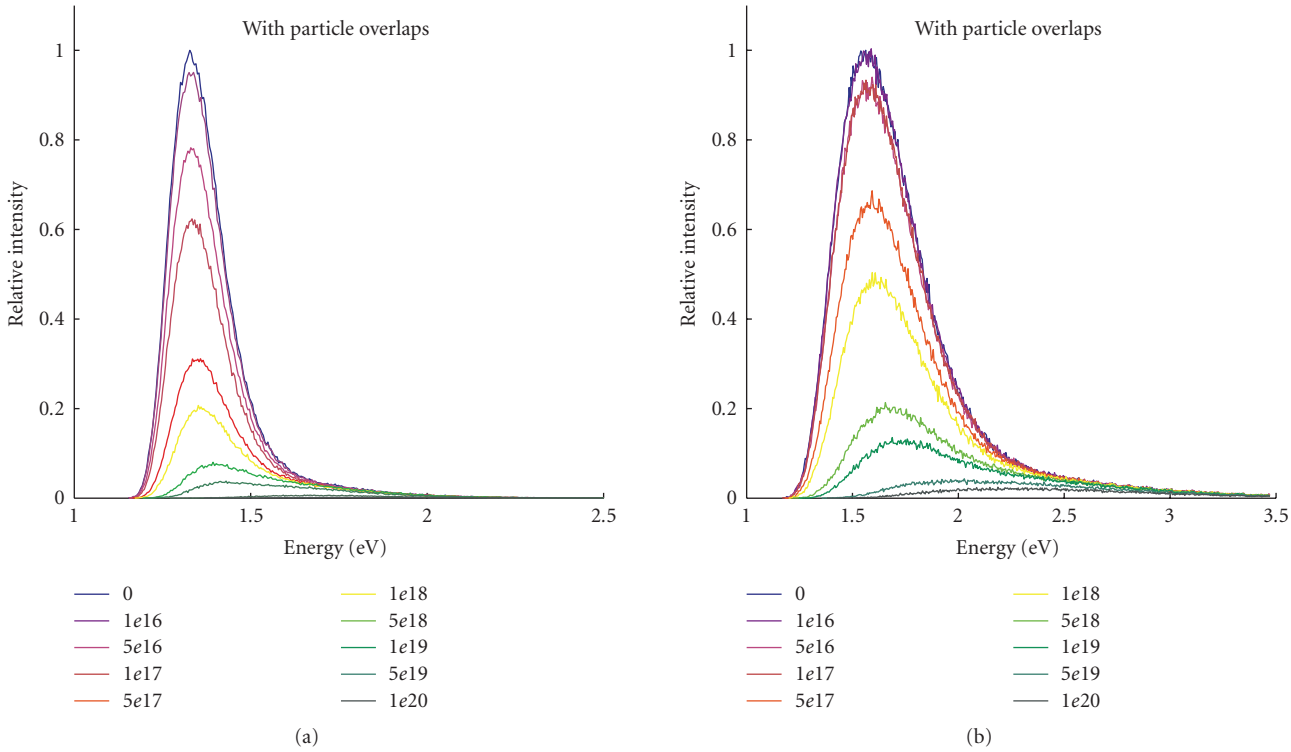

FIGURE 19: PL spectra as a function of surface defect concentration for non-interacting NCs. The spectra in the top panel correspond to $\mu_{\text{radius}} = 2.1\,\text{nm}$, $\text{var}_{\text{radius}} = 0.21\,\text{nm}^2$; the bottom panel is for $\mu_{\text{radius}} = 1.3\,\text{nm}$, $\sigma_{\text{radius}} = 0.38\,\text{nm}$. The legends show the defect concentration in cm^{-3}.

analysis, is not required in order to generate the stretched exponential dynamics, a conclusion that is in agreement with recent experimental results [169].

This is not meant to imply that energy transfer does not occur—in fact, it certainly does occur in most samples as discussed below—but that the shape of the decay curve is in fact governed by the size distribution even in the presence of energy transfer. However, energy transfer will also affect the shape of the decay curve—in the absence of nonradiative processes shifting the decay to longer lifetimes and larger β. In fact, in the absence of nonradiative decay, it is in theory possible to work back from the observed decay to the lifetime distribution using the inverse Laplace transform for the stretched exponential function [170]. From the lifetime distribution one could in principle then work back to the size distribution if $\tau_{pl} \approx \tau_{\text{rad}}$ and the radiative rate model is accurate. If nonradiative processes are included, the values of β and τ are sensitive to the size distribution, filling fraction, and defect concentration. In the discussion below, the first interaction simulation including Forster transfer and tunneling will be performed and its effect on the PL spectrum investigated.

4.3. Interactions

In order to achieve better size control, several studies have formed silicon nanocrystals using a thin film multilayering

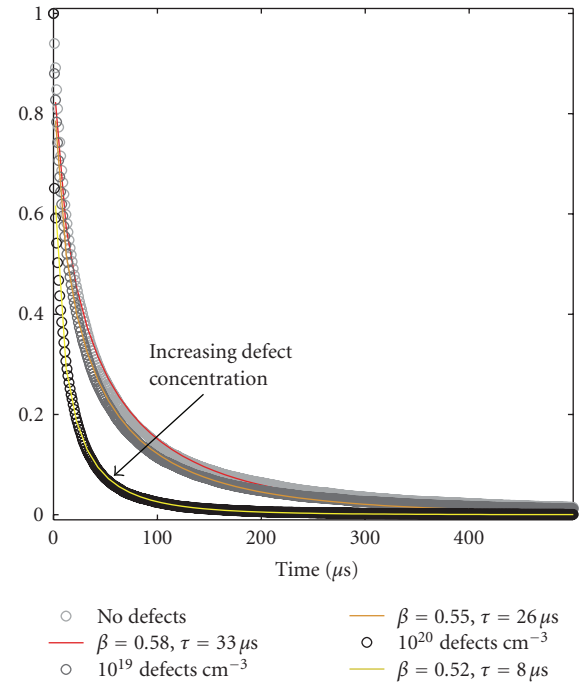

FIGURE 20: Simulated PL decays for a specimen with $\mu_{\text{radius}} = 1.3\,\text{nm}$, $\text{var}_{\text{radius}} = 0.15\,\text{nm}^2$. The lines correspond to defect concentrations of 0, $10^{19}\,\text{cm}^{-3}$, $10^{20}\,\text{cm}^{-3}$. Interactions were not permitted, which minizes the effect of defects.

approach. Instead of depositing a single thick layer of SiO_x, alternating thin layers of SiO_x and SiO_2 were used. In this way, the thin SiO_x layers are isolated from one another by the SiO_2 buffer layers. Upon annealing, silicon clusters crystallize in the SiO_x layers, but the cluster growth occurs only by diffusion within the layer as opposed to three-dimensionally. Although the resulting cluster sizes should clearly be *smaller* than for three-dimensional diffusion in a thick layer of the same composition, it is not immediately clear without more detailed modeling whether the distribution should, in theory, be more narrowly distributed with respect to the mean value. However, narrower distributions have been reported in many cases [171]. Nevertheless, even in apparently monodispersed multilayered samples [165] the PL peak is nearly 200 nm wide at the half maximum.

Through investigating the effect of multilayering of the Si NCs on the luminescence spectrum, it has been observed that the PL spectrum and dynamics from silicon nanocrystals depends on the thickness of both the SiO_2 buffer layers and the active nanocrystal layers, even if the size distributions remain approximately constant [23, 32, 162]. This is evidence of an interaction mechanism operating between the clusters: as the NCs become more isolated—in one direction at least—by the buffer layers, the PL peak shifts to shorter wavelengths and there is a change in the decay dynamics as well, with a possible trend toward higher values of the exponent β. As already discussed, this has been widely interpreted in terms of a kind of excitonic hopping or migration (e.g., see [23]) between clusters, although only more recently have the mechanisms for carrier transfer among Si NCs been more clearly elucidated [30, 160].

There are at least two fundamental means by which closely spaced nanocrystals can exchange charge carriers. The first mechanism is via tunneling of individual electrons or holes from one cluster to another. If the two clusters are approximately the same size (or if the higher levels of a larger cluster overlap with lower levels of a smaller one), then the tunneling is resonant, it is equally probable in either direction, and its rate depends on the negative exponent of the separation distance. Tunneling is well known to occur in silicon clusters and forms the basis of silicon nanocrystal memories [172, 173]. Accurate calculation of the tunneling rate in ensembles of nanocrystals with different energies and spacings is a difficult problem, however. The tunneling rate can be approximated by the Wentzel-Kramers-Brouillin (WKB) approximation, as has been established for the case of double quantum wells [174–176]:

$$w_t = \frac{1}{t_{\text{tunnel}}} = \left(\frac{1}{2d_p}\right)\left(\frac{2E}{m_p}\right)^{1/2} \frac{16E(V-E)(m_p/m_b)}{\left[V+(m_p/m_b-1)E\right]^2} \times \exp\left[-2d_b\left(\frac{2m_b(V-E)}{\hbar^2}\right)^{1/2}\right], \tag{46}$$

where m_b and m_p are the carrier effective masses in the barrier and the particle, d_p and d_b are the particle diameter and barrier thickness, V is the barrier height, and E is the carrier energy. This equation (using the corrected form shown in [160]) has previously been employed to estimate tunneling rates between *asymmetric* quantum wells [176], despite the fact that (46) is strictly applicable only to the resonant case.

If the energy levels of adjacent clusters are mismatched, then tunneling must be "assisted" by emission or absorption of phonons. The tunneling rate dependence on the energy gap, ΔE, and the phonon energies (within the clusters and in the SiO_2 matrix) for these mechanisms is not well known and may need to be estimated experimentally if sufficiently narrow size distributions can be obtained. Recently, computer simulations showed [160] that a large Stokes shift between absorption and emission in the specimen as a whole can occur as a result of tunneling between nanocrystals although, as for the quantum well case, (46) was used without accounting for phonon-assisted tunneling.

The second fundamental interaction mechanism is resonance energy transfer, or "Forster transfer" [177]. In this mechanism, electron-hole pairs may "migrate" from particle to particle by a dipole-dipole or higher-order multipole coupling, that is, the Forster process—which has already been established for the case of CdSe nanocrystals [178]. Others have shown that it applies to silicon nanocrystals also [30], although due to the indirect gap the rates can be much different (typically smaller) than for CdSe. Forster transfer is the basis for fluorescence resonance energy transfer (FRET) microscopy, and has been widely investigated in the case of interactions amongst the rare earth ions [179]. The distance dependence of the transition dipole transfer rate, w_d, is given by $w_d = w_{\text{PL}}(R_0/r)^6$, where w_{PL} is the PL rate, R_0 is the distance at which the transfer rate and the PL rate are equal, and r is the distance between the edges of the particles. R_0 itself depends on the spectral overlap integral between the donor (D) and acceptor (A) clusters, and is, therefore, technically different for any pair of nanocrystals undergoing this process. Previous work in CdSe nanocrystals has assumed that the energy levels must be resonant for the Forster transfer to occur [178], however this is not strictly true: phonon-assisted Forster transfer has been calculated for the rare earth ions and should apply to nanocrystals as well. In the Miyakawa-Dexter theory [180], the resonant Forster rate is modified by considering the electron-phonon coupling parameters in the density-of-states function for the donor and activator ions. In this way, one obtains [180]:

$$w_{\text{dip}} = w_{pl}\left(\frac{R_0}{r}\right)^6 \exp(-\beta\Delta E), \tag{47}$$

where β depends on the electron-phonon coupling strength, and its value can be extracted from a plot of the transfer rate versus ΔE in silicate glass. From the data provided in [181], a rough estimate gives $\alpha = 0.0018$ for rare earth ions embedded in SiO_2, where α indicates internal transitions and is about twice the value of β [180]. Unfortunately, the value of β is much more difficult to obtain experimentally for silicon NCs, as a result of the size distributions (i.e., every NC is slightly different; whereas all rare earth ions of the same type have identical properties).

The Miyakawa-Dexter model has been widely discussed and applied extensively in the case of transfer between

different rare earth ions [182–184]. In the present case, one may assume that the energy difference is lost to phonons in the surrounding silicate glass, as would be the case for isolated "point" dipoles such as the rare earth ions. As the energy gap grows, the transfer rate decreases exponentially, and experimentally, for rare earth ions at least, this trend shows little variation despite the many simplifications in the Miyakawa-Dexter model [185]. The effective Forster distance, R_0, is more difficult to obtain, since it is not practical to calculate the overlap integral (including phonon sidebands) for every possible pair of interacting particles in a sample. Therefore, an experimental approach is taken to approximate a single R_0 value for all pairs of particles. By varying the distance between layers of interacting particles and using the geometrical constraints imposed by interacting layers (as opposed to two point dipoles) [186], an estimated value of $R_0 = 5$ nm was used in the simulations. Obviously, this is a significant simplification and it must be stressed that the results remain approximate until phonon-assisted multipole transfer between all possible pairs of NCs can be calculated in a reasonable way.

The simulation setup was done exactly as described previously: every particle was populated with a single electron-hole pair at time $t = 0$. This time, the effect of nonradiative traps was not included in order to show only the energy migration effects. Next, for every nanocluster the probabilities associated with each of the four processes described above (radiative decay, nonradiative decay, tunneling, and Forster transfer) were calculated in random order (the NCs themselves are also checked randomly) and compared to a flat-probability random number between 0 and 1 to determine whether one of these four events occurred. When the calculation started, the simulation timestep was 1×10^{-12} s. After iterating through all the particles, the time increments by one picosecond and the process repeats. If ten complete iterations through all the clusters (in randomized order each time) produce no events of any kind, the timestep is multiplied by a factor of ten. In this way, it is possible to overcome the otherwise impossible computational limits associated with the vastly different rates for the different processes. The simulation ends when there are no electron-hole pairs left. When a particle radiates, the energy of the outgoing photon is stored for the spectral output function, and the time is recorded in order to plot the decay of the luminescence. Finally, a set of tests were performed to find the minimum sample size for which edge effects (due to the finite box size) became unobservable. A simulation of 5,000 particles was found to provide sufficiently short computation time (~12 hours on a 2.6 GHz CPU) and no observable edge effects. Auger effects were not simulated, which effectively approximates the behavior of a lightly pumped ensemble.

Figure 21 shows the PL spectrum with and without the Forster and tunneling "energy migration" interactions. In the first few nanoseconds, numerous tunneling events and dipole-dipole interactions occurred. The rates for these processes for adjacent nanocrystals are many orders of magnitude faster than the radiative decay processes. Some nonradiative trapping can also occur early on in the simulation. Even after only a few picoseconds, there was already

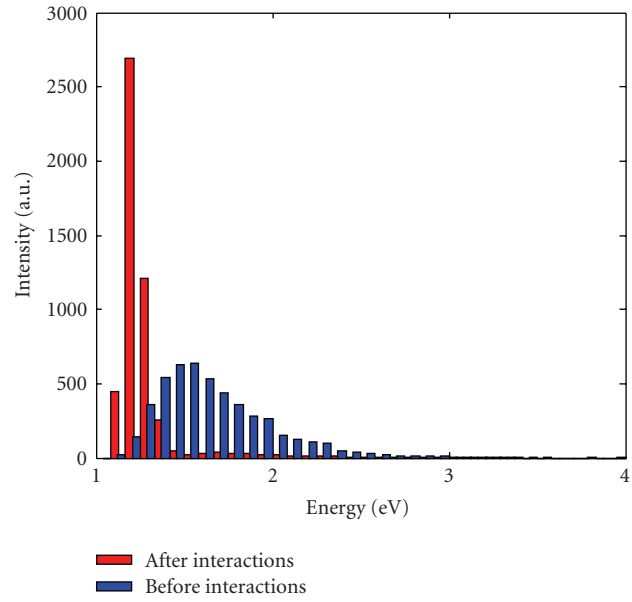

Figure 21: Effect of carrier migration on the PL histogram of a silicon NC ensemble with a lognormal distribution $S = 0.21$, $M = 0.74$, and volume fill = 35%. The PL spectrum is strongly redshifted as a result of tunneling and Forster transfer in this densely packed ensemble. For this simulation, there were no non-radiative defects and infinte barriers were assumed. The "after interactions" result agrees reasonably well with the observed CW PL from a specimen with the same size distribution and volume fill [47].

a small fraction of charged nanocrystals due to electron or hole tunneling events. Many nanocrystals had no remaining charge carriers, and many others—predominantly the larger ones—had multiple electron-hole pairs. After 500 ns, many thousands of tunneling and dipole events occurred and most of the smaller clusters were devoid of charge carriers. In the microsecond timescale, radiative decay joins the longer-range energy transfer events, and by 100 microseconds only a few excited nanocrystals remained. The long wavelength of the emitting states (compared to absorption)—as well as a decrease in the overall skewness of the PL peak—in dense ensembles of Si NCs can originate predominantly from energy migration, indicating that the large Stokes shift in ensembles of Si NCs can be attributed, at least in part, to these effects. We have also found that the degree of "stretching" of the PL decay depends on the resulting ensemble of particles with electron-hole pairs; in the absence of nonradiative effects the PL lifetime is longer but if defects are introduced the PL lifetime can be dramatically shorter in the presence of energy migration, due to the greater statistical probability for defects to occur on larger NCs. Based on the initial results presented here, it would seem that the combination of theory with computational simulations may be one of the best tools to obtain a more thorough understanding of the complicated and controversial luminescence behavior of ensembles of silicon clusters.

At this point, although instructive, the simulations have obvious limitations that we are currently working to overcome. For example, we have not incorporated the

effects of Si=O surface bonds, which again may cause the simulated spectra to peak at wavelengths slightly too short, especially for smaller NCs. An obvious limitation of the model is the estimate of a single value of R_0 for all Forster interactions. The fact that phonon-assisted Forster processes among silicon NCs remain beyond theoretical scope [30], required a further assumption that the phonon-assisted rate had a similar dependence on ΔE as for the case for rare-earth ions in silicate glass. Higher-order multipole interactions were also ignored. Finally, unlike the case in which infinite barriers were assumed [160], here the resulting spectra are narrower and redden than observed experimentally.

Nevertheless, the implications of these simulations are clear. First, the two energy transfer mechanisms dominate the PL spectrum when the clusters are separated by less than 2 nm, and can still be significant in the case of Forster transfer over distances of 5 nm or more. Therefore, in most of the experimental work reported to date, NC-NC interactions strongly affect the PL spectrum. Multilayer simulations such as that shown in Figure 18 have also been performed, and the results are consistent with the experimentally observed spectral blueshift and increased lifetime in multilayered samples. The decay exponent β shows a more complicated behavior however; its value depends on the distribution of lifetimes which in turn depends on the size distribution and the nonradiative defect concentration. Next, in most samples the largest clusters act as depressions in the energy landscape and can attract numerous charge carriers. Under high pump rates, therefore, the Auger problem can become significant when the clusters are reasonably closely separated. Next, the simulations can easily be extended to model the sensitizing action of the NCs on erbium ions; this work is currently ongoing and uses the Forster mechanism of energy transfer. The results seem consistent with the reports of optical gain (ASE) in very short timescales before significant amount of energy transfer can occur (as long as the size distribution is sufficiently narrow to have a narrow enough gain profile) but for CW stimulated emission the NCs must be sufficiently well separated to prevent carrier migration and buildup on the largest clusters. The largest NCs are also the ones most likely to contain a defect, so their effects on the emission spectrum and gain profile are extremely strong in most samples where carrier interactions occur. Therefore, in the final section of this paper we briefly discuss the controversial observations of optical gain in silicon nanocrystals, and the implications of the theoretical results in Sections 1–3 and the simulations of Section 4 for the development of photonic devices relating to stimulated emission in silicon nanocrystals.

4.4. Stimulated emission in Si NCs

There have been numerous recent reports of optical gain in silicon nanocrystals [165, 187–189], and stimulated emission was reported in [190], although to our knowledge the results are not fully understood. Many of these studies deduced the presence of gain by analyzing data from the variable strip length (VSL) technique [191]. This method has been discussed in great detail in the literature, owing to the many possible sources of error. In general, a planar waveguide film containing silicon nanocrystals is optically pumped from above (parallel to the specimen surface normal). The pump laser beam is first incident on a variable-length slit, such that only a diffraction-limited strip of the sample is pumped. The waveguided PL signal is then collected from the edge of the specimen in the direction parallel to the axis of the excitation strip. The signature of optical gain is a superlinear increase in the PL intensity (marked by a distinct transition) for constant pump flux as the strip is lengthened. This is due to the stimulated emission from excited nanocrystals interacting with photons originally emitted at the farther end of the excitation strip. This method, along with some corrections, has been one of the most widely used methods to support optical gain in Si NCs. The other method that has been used, although somewhat less extensively, is the standard pump-probe technique. In that case, the transmission of a probe beam is measured as a function of the probe power, with the transition from loss to gain marked by a shift from positive to negative absorption of the pump. This method has been used both for Si NC waveguides and in single-pass measurements.

The presence (or absence) of SE in Si NCs is a subject of much debate. After the initial report [5], which used both the VSL and the single-pass pump-probe methods to report a net modal gain for a silicon nanocrystal film of $100\,\mathrm{cm}^{-1}$, a net material gain of $10^4\,\mathrm{cm}^{-1}$, and a gain cross section per NC of $\sim 10^{-16}\,\mathrm{cm}^2$, numerous groups have searched for optical gain in ensembles of Si NCs. The results of these investigations have not been entirely consistent. Currently, there seems to be some possible evidence in favor of SE in an Auger-limited time window of a few ns after intense pulsed excitation, with gain cross sections per NC of $\sim 10^{-16}\,\mathrm{cm}^2$ in the extreme short wavelength side of the broad emission band [189]. However, in comparison to the case for CdSe NCs, where there is clear and unequivocal observations of SE (e.g., marked by a sudden superlinear increase of PL intensity with pumping power in a narrow wavelength range), in the case of Si NCs the signatures of SE have been extracted from fairly elaborate and complicated experiments, and the results have shown significant specimen-to-specimen variation. A brief examination of the limiting factors and key specimen requirements for SE in ensembles of silicon NCs would be of use with the ultimate objective demonstrating, unequivocally, stimulated emission in nanocrystalline silicon.

Gain profile

The calculations discussed in Sections 1–3 indicate several key factors relating to optical gain in Si NCs. First, for size distributions produced by standard physical vapor deposition or ion implantation methods (including multilayering) the gain profile becomes extremely wide. This reduces the gain coefficient and the gain cross section per NC in the sample. Dal Negro et al. [187], for example, reported a gain coefficient of $1600 \pm 300\,\mathrm{cm}^{-1}$ at $\lambda = 750\,\mathrm{nm}$, with a gain cross section at this wavelength of $3 \times 10^{-16}\,\mathrm{cm}^2$ per NC. Since the overall PL spectra generally peak at longer wavelengths, only a small fraction of the NCs may actually emit within the reported gain window. Most of the nanocrystals, therefore, may not contribute to SE

and are in fact, detrimental as a result of confined carrier absorption, scattering, and other loss mechanisms they can cause. If Si NCs could be prepared with a size distribution similar to that for CdSe (e.g., 5% standard deviation), the theoretical gain coefficient per nanocrystal in the specimen as a whole could increase by a fairly large factor, simply because a greater number of NCs could contribute to the overall gain at the peak wavelength. Therefore, true monodispersivity (i.e., overall emission profile controlled by homogeneous broadening) is likely to be a requirement for producing SE in ensembles of Si NCs.

Secondly, the size distribution presents an inherent problem for laser excitation of the specimen. With the exception of erbium doped waveguides that used LED excitation [192], SE or gain is reported as a result of pumping the sample with a laser. Laser excitation implies a narrow excitation energy window, and only NCs that happen to have a transition within that window will be absorbing. In a given sample with a wide distribution, therefore, many of the NCs may not absorb and cannot contribute to the overall specimen gain. Furthermore, these "unexcited" NCs can enhance the energy migration or other undesired effects discussed above.

The cluster-cluster energy transfer mechanisms found to be important in the overall luminescence spectrum also have implications for the presence of SE in ensembles of Si NCs. Generally, a high-pump rate is necessary to observe the transition from loss to gain. Under such high rates, one can assume a relatively large number of excitons per NC (we hesitate somewhat to suggest a number as high as 100) [5] but at least 1 exciton per NC is readily possible. In this case, charge carriers will be rapidly redistributed through the tunneling and Forster mechanisms, on the sub-nanosecond time scale for a typical volume filling fraction of NCs (the volume fraction ultimately controls the average NC-NC spacing). Therefore, in a short time after the initial pump pulse, one has the accumulation of charge carriers on the largest NCs as a result of tunneling and Forster interactions. This drastically decreases the number of NCs that can contribute to the gain spectrum and can lead to enhanced nonradiative trapping and undesirable Auger interactions. This may be one reason that gain may only occur in very short timescales, as suggested in several recent experimental works [189], and only in certain specimens but not in others. In such cases, gain may only build up before the energy migration processes have occurred, and will be very susceptible to the average NC-NC spacing (and size distribution, as above) from specimen to specimen. The fact that the gain, if present, occurs on the short-wavelength side of the PL band is also consistent with the idea that the gain occurs before the charge carriers transfer to the larger and "redder" nanoclusters. By increasing the NC-NC spacing it should be possible to limit the energy migration problem, due to the strong distance dependence of the main processes. This may be accomplished by, for example, freeing the Si NCs via an HF etch and redepositing them at a known (low) filling fraction, an idea we are currently exploring. Other methods are also possible.

Additionally, the level degeneracies calculated in Section 3 imply a further key limiting factor for SE in silicon nanocrystals. With a two-fold degeneracy or more, more than 1 exciton per NC must be present, on average, in order to switch from loss to gain, which in turn raises the problem of the Auger interactions. This number becomes higher as the degeneracy of the electron and hole levels increases. In the case of CdSe NCs, Klimov et al. [193] have shown that one way to avoid this problem is to separate electrons and holes in a core-shell nanostructure, thereby creating a large crystal-field shift of the absorption spectrum. Such problems (and solutions) may well apply to Si NCs also.

5. CONCLUSION

There is now an enormous wealth of data on ensembles of silicon nanoclusters. The difficulties in understanding the optical properties of these materials are caused by the indirect gap of silicon, the large homogeneous, and inhomogeneous broadening, the possible effects of radiative centers and nonradiative traps, the cluster size dependence of the lifetimes, and energy transfer. All these processes must be considered when evaluating a luminescence spectrum; it is insufficient to study the luminescence as a function of cluster size only, although size undoubtedly plays a role. Unfortunately, owing to the complexity of the materials, there are many contradictory observations and much uncertainty in the literature. We hope that, with this paper, we have been able to summarize some of the main theoretical and computational results that should help to work out the problems and issues with our understanding of ensembles of silicon NCs. We hope that the combination of theory and simulation, new single particle spectroscopies [20], and new synthesis methods [194] will eventually lead to unequivocal and readily reproducible reports of stimulated emission in Si NCs.

ACKNOWLEDGMENTS

A. Meldrum and R. Lockwood acknowledge and thank iCORE and NSERC. V. A. Belyakov and V. A. Burdov acknowledge RFBR, Russian Ministry of Education and Science ("Development of Scientific Potential of the High School" program), and the "Dynasty" foundation (Russia) for the partial financial support of this work.

REFERENCES

[1] H. Takagi, H. Ogawa, Y. Yamazaki, A. Ishizaki, and T. Nakagiri, "Quantum size effects on photoluminescence in ultrafine Si particles," *Applied Physics Letters*, vol. 56, no. 24, pp. 2379–2380, 1990.

[2] L. T. Canham, "Silicon quantum wire array fabrication by electrochemical and chemical dissolution of wafers," *Applied Physics Letters*, vol. 57, no. 10, pp. 1046–1048, 1990.

[3] P. D. J. Calcott, K. J. Nash, L. T. Canham, M. J. Kane, and D. Brumhead, "Identification of radiative transitions in highly porous silicon," *Journal of Physics: Condensed Matter*, vol. 5, no. 7, pp. L91–L98, 1993.

[4] P. D. J. Calcott, K. J. Nash, L. T. Canham, M. J. Kane, and D. Brumhead, "Spectroscopic identification of the

luminescence mechanism of highly porous silicon," *Journal of Luminescence*, vol. 57, no. 1–6, pp. 257–269, 1993.

[5] L. Pavesi, L. Dal Negro, C. Mazzoleni, G. Franzò, and F. Priolo, "Optical gain in silicon nanocrystals," *Nature*, vol. 408, no. 6811, pp. 440–444, 2000.

[6] D. Kovalev, H. Heckler, G. Polisski, and F. Koch, "Optical properties of Si nanocrystals," *Physica Status Solidi B*, vol. 215, no. 2, pp. 871–932, 1999.

[7] L. Khriachtchev, M. Räsänen, S. Novikov, O. Kilpelä, and J. Sinkkonen, "Raman scattering from very thin Si layers of Si/SiO_2 superlattices: experimental evidence of structural modification in the 0.8–3.5 nm thickness region," *Journal of Applied Physics*, vol. 86, no. 10, pp. 5601–5608, 1999.

[8] M. V. Wolkin, J. Jorne, P. M. Fauchet, G. Allan, and C. Delerue, "Electronic states and luminescence in porous silicon quantum dots: the role of oxygen," *Physical Review Letters*, vol. 82, no. 1, pp. 197–200, 1999.

[9] A. B. Filonov, S. Ossicini, F. Bassani, and F. Arnaud d'Avitaya, "Effect of oxygen on the optical properties of small silicon pyramidal clusters," *Physical Review B*, vol. 65, no. 19, Article ID 195317, 9 pages, 2002.

[10] D. I. Tetelbaum, I. A. Karpovich, M. V. Stepikhova, V. G. Shengurov, K. A. Markov, and O. N. Gorshkov, "Characteristics of photoluminescence in SiO_2 with Si nanoinclusions produced by ion implantation," *Surface Investigation X-Ray, Synchrotron and Neutron Techniques*, vol. 14, no. 5, pp. 601–604, 1998.

[11] M. Fujii, A. Mimura, S. Hayashi, and K. Yamamoto, "Photoluminescence from Si nanocrystals dispersed in phosphosilicate glass thin films: improvement of photoluminescence efficiency," *Applied Physics Letters*, vol. 75, no. 2, pp. 184–186, 1999.

[12] A. Miura, M. Fujii, S. Hayashi, D. Kovalev, and F. Koch, "Photoluminescence and free-electron absorption in heavily phosphorus-doped Si nanocrystals," *Physical Review B*, vol. 62, no. 19, pp. 12625–12627, 2000.

[13] M. Fujii, A. Mimura, S. Hayashi, Y. Yamamoto, and K. Murakami, "Hyperfine structure of the electron spin resonance of phosphorus-doped Si nanocrystals," *Physical Review Letters*, vol. 89, no. 20, Article ID 206805, 4 pages, 2002.

[14] M. Fujii, K. Toshikiyo, Y. Takase, Y. Yamaguchi, and S. Hayashi, "Below bulk-band-gap photoluminescence at room temperature from heavily P- and B-doped Si nanocrystals," *Journal of Applied Physics*, vol. 94, no. 3, pp. 1990–1995, 2003.

[15] M. Fujii, Y. Yamaguchi, Y. Takase, K. Ninomiya, and S. Hayashi, "Control of photoluminescence properties of Si nanocrystals by simultaneously doping *n*- and *p*-type impurities," *Applied Physics Letters*, vol. 85, no. 7, pp. 1158–1160, 2004.

[16] G. A. Kachurin, S. G. Cherkova, V. A. Volodin, et al., "Implantation of P ions in SiO_2 layers with embedded Si nanocrystals," *Nuclear Instruments and Methods in Physics Research B*, vol. 222, no. 3-4, pp. 497–504, 2004.

[17] M. Fujii, Y. Yamaguchi, Y. Takase, K. Ninomiya, and S. Hayashi, "Photoluminescence from impurity codoped and compensated Si nanocrystals," *Applied Physics Letters*, vol. 87, no. 21, Article ID 211919, 3 pages, 2005.

[18] G. A. Kachurin, S. G. Cherkova, V. A. Volodin, D. M. Marin, D. I. Tetelbaum, and H. Becker, "Effect of boron ion implantation and subsequent anneals on the properties of Si nanocrystals," *Semiconductors*, vol. 40, no. 1, pp. 72–78, 2006.

[19] J. Valenta, R. Juhasz, and J. Linnros, "Photoluminescence spectroscopy of single silicon quantum dots," *Applied Physics Letters*, vol. 80, no. 6, pp. 1070–1072, 2002.

[20] I. Sychugov, R. Juhasz, J. Valenta, and J. Linnros, "Narrow luminescence linewidth of a silicon quantum dot," *Physical Review Letters*, vol. 94, no. 8, Article ID 087405, 4 pages, 2005.

[21] F. Priolo, G. Franzò, D. Pacifici, V. Vinciguerra, F. Iacona, and A. Irrera, "Role of the energy transfer in the optical properties of undoped and Er-doped interacting Si nanocrystals," *Journal of Applied Physics*, vol. 89, no. 1, pp. 264–272, 2001.

[22] I. Balberg, E. Savir, and J. Jedrzejewski, "The mutual exclusion of luminescence and transport in nanocrystalline silicon networks," *Journal of Non-Crystalline Solids*, vol. 338–340, pp. 102–105, 2004.

[23] J. Heitmann, F. Müller, L. Yi, M. Zacharias, D. Kovalev, and F. Eichhorn, "Excitons in Si nanocrystals: confinement and migration effects," *Physical Review B*, vol. 69, no. 19, Article ID 195309, 7 pages, 2004.

[24] T. Kawazoe, K. Kobayashi, and M. Ohtsu, "Optical nanofountain: a biomimetic device that concentrates optical energy in a nanometric region," *Applied Physics Letters*, vol. 86, no. 10, Article ID 103102, 3 pages, 2005.

[25] T. Förster, "Versuche zum zwischenmolekularen. Übergang von elektronenanregungsenergie," *Zeitschrift für Elektrochemie*, vol. 53, pp. 93–100, 1949.

[26] T. Förster, "Experimentelle und theoretische Untersuchung des zwischenmolekularen Übergangs von Elektronenanregungsenergie," *Zeitschrift für Naturforschung A*, vol. 4, pp. 321–327, 1949.

[27] D. L. Dexter, "A theory of sensitized luminescence in solids," *The Journal of Chemical Physics*, vol. 21, no. 5, pp. 836–850, 1953.

[28] C. R. Kagan, C. B. Murray, M. Nirmal, and M. G. Bawendi, "Electronic energy transfer in CdSe quantum dot solids," *Physical Review Letters*, vol. 76, no. 9, pp. 1517–1520, 1996.

[29] S. A. Crooker, J. A. Hollingsworth, S. Tretiak, and V. I. Klimov, "Spectrally resolved dynamics of energy transfer in quantum-dot assemblies: towards engineered energy flows in artificial materials," *Physical Review Letters*, vol. 89, no. 18, Article ID 186802, 4 pages, 2002.

[30] G. Allan and C. Delerue, "Energy transfer between semiconductor nanocrystals: validity of Förster's theory," *Physical Review B*, vol. 75, no. 19, Article ID 195311, 8 pages, 2007.

[31] Y. Kanemitsu, "Photoluminescence spectrum and dynamics in oxidized silicon nanocrystals: a nanoscopic disorder system," *Physical Review B*, vol. 53, no. 20, pp. 13515–13520, 1996.

[32] J. Linnros, N. Lalic, A. Galeckas, and V. Grivickas, "Analysis of the stretched exponential photoluminescence decay from nanometer-sized silicon crystals in SiO_2," *Journal of Applied Physics*, vol. 86, no. 11, pp. 6128–6134, 1999.

[33] M. Dovrat, Y. Goshen, J. Jedrzejewski, I. Balberg, and A. Sa'ar, "Radiative versus nonradiative decay processes in silicon nanocrystals probed by time-resolved photoluminescence spectroscopy," *Physical Review B*, vol. 69, no. 15, Article ID 155311, 8 pages, 2004.

[34] F. Trojánek, K. Neudert, M. Bittner, and P. Malý, "Picosecond photoluminescence and transient absorption in silicon nanocrystals," *Physical Review B*, vol. 72, no. 7, Article ID 075365, 6 pages, 2005.

[35] R. J. Walters, J. Kalkman, A. Polman, H. A. Atwater, and M. J. A. de Dood, "Photoluminescence quantum efficiency of dense silicon nanocrystal ensembles in Si O_2," *Physical Review B*, vol. 73, no. 13, Article ID 132302, 4 pages, 2006.

[36] C. Delerue, G. Allan, C. Reynaud, O. Guillois, G. Ledoux, and F. Huisken, "Multiexponential photoluminescence decay in

indirect-gap semiconductor nanocrystals," *Physical Review B*, vol. 73, no. 23, Article ID 235318, 4 pages, 2006.

[37] A. Meldrum, R. F. Haglund Jr., L. A. Boatner, and C. W. White, "Nanocomposite materials formed by ion implantation," *Advanced Materials*, vol. 13, no. 19, pp. 1431–1444, 2001.

[38] A. Meldrum, L. A. Boatner, and C. W. White, "Nanocomposites formed by ion implantation: recent developments and future opportunities," *Nuclear Instruments and Methods in Physics Research B*, vol. 178, no. 1–4, pp. 7–16, 2001.

[39] K. S. Zhuravlev, A. M. Gilinsky, and A. Yu. Kobitsky, "Mechanism of photoluminescence of Si nanocrystals fabricated in a SiO_2 matrix," *Applied Physics Letters*, vol. 73, no. 20, pp. 2962–2964, 1998.

[40] Y. Kanemitsu, N. Shimizu, T. Komoda, P. L. F. Hemment, and B. J. Sealy, "Photoluminescent spectrum and dynamics of Si^+-ion-implanted and thermally annealed SiO_2 glasses," *Physical Review B*, vol. 54, no. 20, pp. R14329–R14332, 1996.

[41] S. Guha, "Characterization of Si^+ ion-implanted SiO_2 films and silica glasses," *Journal of Applied Physics*, vol. 84, no. 9, pp. 5210–5217, 1998.

[42] L. Dal Negro, M. Cazzanelli, L. Pavesi, et al., "Dynamics of stimulated emission in silicon nanocrystals," *Applied Physics Letters*, vol. 82, no. 26, pp. 4636–4638, 2003.

[43] L. Tsybeskov, K. D. Hirschman, S. P. Duttagupta, et al., "Nanocrystalline-silicon superlattice produced by controlled recrystallization," *Applied Physics Letters*, vol. 72, no. 1, pp. 43–45, 1998.

[44] M. Zacharias, J. Heitmann, R. Scholz, U. Kahler, M. Schmidt, and J. Bläsing, "Size-controlled highly luminescent silicon nanocrystals: a SiO/SiO_2 superlattice approach," *Applied Physics Letters*, vol. 80, no. 4, pp. 661–663, 2002.

[45] M. H. Nayfeh, S. Rao, N. Barry, et al., "Observation of laser oscillation in aggregates of ultrasmall silicon nanoparticles," *Applied Physics Letters*, vol. 80, no. 1, pp. 121–123, 2002.

[46] A. Meldrum, A. Hryciw, A. N. MacDonald, et al., "Photoluminescence in the silicon-oxygen system," *Journal of Vacuum Science and Technology A*, vol. 24, no. 3, pp. 713–717, 2006.

[47] J. Wang, X. F. Wang, Q. Li, A. Hryciw, and A. Meldrum, "The microstructure of SiO thin films: from nanoclusters to nanocrystals," *Philosophical Magazine*, vol. 87, no. 1, pp. 11–27, 2007.

[48] G. Ledoux, J. Gong, F. Huisken, O. Guillois, and C. Reynaud, "Photoluminescence of size-separated silicon nanocrystals: confirmation of quantum confinement," *Applied Physics Letters*, vol. 80, no. 25, pp. 4834–4836, 2002.

[49] T.-Y. Kim, N.-M. Park, K.-H. Kim, et al., "Quantum confinement effect of silicon nanocrystals in situ grown in silicon nitride films," *Applied Physics Letters*, vol. 85, no. 22, pp. 5355–5357, 2004.

[50] P. M. Fauchet, "Light emission from Si quantum dots," *Materials Today*, vol. 8, no. 1, pp. 26–33, 2005.

[51] Y. Kanemitsu, S. Okamoto, M. Otobe, and S. Oda, "Photoluminescence mechanism in surface-oxidized silicon nanocrystals," *Physical Review B*, vol. 55, no. 12, pp. R7375–R7378, 1997.

[52] Y. Kanzawa, T. Kageyama, S. Takeoka, M. Fujii, S. Hayashi, and K. Yamamoto, "Size-dependent near-infrared photoluminescence spectra of Si nanocrystals embedded in SiO_2 matrices," *Solid State Communications*, vol. 102, no. 7, pp. 533–537, 1997.

[53] B. Garrido Fernandez, M. López, C. García, et al., "Influence of average size and interface passivation on the spectral emission of Si nanocrystals embedded in SiO_2," *Journal of Applied Physics*, vol. 91, no. 2, pp. 798–807, 2002.

[54] T. van Buuren, L. N. Dinh, L. L. Chase, W. J. Siekhaus, and L. J. Terminello, "Changes in the electronic properties of Si nanocrystals as a function of particle size," *Physical Review Letters*, vol. 80, no. 17, pp. 3803–3806, 1998.

[55] S. Schuppler, S. L. Friedman, M. A. Marcus, et al., "Size, shape, and composition of luminescent species in oxidized Si nanocrystals and H-passivated porous Si," *Physical Review B*, vol. 52, no. 7, pp. 4910–4925, 1995.

[56] B. Garrido, M. López, O. González, A. Pérez-Rodríguez, J. R. Morante, and C. Bonafos, "Correlation between structural and optical properties of Si nanocrystals embedded in SiO_2: the mechanism of visible light emission," *Applied Physics Letters*, vol. 77, no. 20, pp. 3143–3145, 2000.

[57] S. Takeoka, M. Fujii, and S. Hayashi, "Size-dependent photoluminescence from surface-oxidized Si nanocrystals in a weak confinement regime," *Physical Review B*, vol. 62, no. 24, pp. 16820–16825, 2000.

[58] M. Lannoo, C. Delerue, and G. Allan, "Theory of radiative and nonradiative transitions for semiconductor nanocrystals," *Journal of Luminescence*, vol. 70, no. 1–6, pp. 170–184, 1996.

[59] C. Garcia, B. Garrido, P. Pellegrino, et al., "Size dependence of lifetime and absorption cross section of Si nanocrystals embedded in SiO_2," *Applied Physics Letters*, vol. 82, no. 10, pp. 1595–1597, 2003.

[60] L. Dal Negro, M. Cazzanelli, N. Daldosso, et al., "Stimulated emission in plasma-enhanced chemical vapour deposited silicon nanocrystals," *Physica E*, vol. 16, no. 3-4, pp. 297–308, 2003.

[61] M. Fujii, D. Kovalev, B. Goller, S. Minobe, S. Hayashi, and V. Yu. Timoshenko, "Time-resolved photoluminescence studies of the energy transfer from excitons confined in Si nanocrystals to oxygen molecules," *Physical Review B*, vol. 72, no. 16, Article ID 165321, 8 pages, 2005.

[62] S. Miura, T. Nakamura, M. Fujii, M. Inui, and S. Hayashi, "Size dependence of photoluminescence quantum efficiency of Si nanocrystals," *Physical Review B*, vol. 73, no. 24, Article ID 245333, 5 pages, 2006.

[63] A. Yu. Kobitski, K. S. Zhuravlev, H. P. Wagner, and D. R. T. Zahn, "Self-trapped exciton recombination in silicon nanocrystals," *Physical Review B*, vol. 63, no. 11, Article ID 115423, 5 pages, 2001.

[64] A. Sa'ar, M. Dovrat, J. Jedrzejewski, and I. Balberg, "Optical inter- and intra-band transitions in silicon nanocrystals: the role of surface vibrations," *Physica E*, vol. 38, no. 1-2, pp. 122–127, 2007.

[65] F. A. Reboredo, A. Franceschetti, and A. Zunger, "Excitonic transitions and exchange splitting in Si quantum dots," *Applied Physics Letters*, vol. 75, no. 19, pp. 2972–2974, 1999.

[66] F. A. Reboredo, A. Franceschetti, and A. Zunger, "Dark excitons due to direct Coulomb interactions in silicon quantum dots," *Physical Review B*, vol. 61, no. 19, pp. 13073–13087, 2000.

[67] D. H. Feng, Z. Z. Xu, T. Q. Jia, X. X. Li, and S. Q. Gong, "Quantum size effects on exciton states in indirect-gap quantum dots," *Physical Review B*, vol. 68, no. 3, Article ID 035334, 7 pages, 2003.

[68] H.-Ch. Weissker, J. Furthmüller, and F. Bechstedt, "Structure- and spin-dependent excitation energies and lifetimes of Si and Ge nanocrystals from *ab initio* calculations," *Physical Review B*, vol. 69, no. 11, Article ID 115310, 8 pages, 2004.

[69] D. I. Tetelbaum, O. N. Gorshkov, S. A. Trushun, D. G. Revin, D. M. Gaponova, and W. Eckstein, "Enhancement of luminescence in ion implanted Si quantum dots in SiO_2 matrix by means of dose alignment and doping," *Nanotechnology*, vol. 11, no. 4, pp. 295–297, 2000.

[70] D. I. Tetelbaum, S. A. Trushin, V. A. Burdov, A. I. Golovanov, D. G. Revin, and D. M. Gaponova, "Influence of phosphorus and hydrogen ion implantation on the photoluminescence of SiO_2 with Si nanoinclusions," *Nuclear Instruments and Methods in Physics Research B*, vol. 174, no. 1-2, pp. 123–129, 2001.

[71] D. I. Tetelbaum, O. N. Gorshkov, V. A. Burdov, et al., "The influence of P^+, B^+, and N^+ ion implantation on the luminescence properties of the SiO_2: nc-Si system," *Physics of the Solid State*, vol. 46, no. 1, pp. 17–21, 2004.

[72] A. N. Mikhaylov, D. I. Tetelbaum, V. A. Burdov, et al., "Effect of ion doping with donor and acceptor impurities on intensity and lifetime of photoluminescence from SiO_2 films with silicon quantum dots," *Journal of Nanoscience and Nanotechnology*, vol. 8, no. 2, pp. 780–788, 2008.

[73] V. A. Belyakov and V. A. Burdov, "Valley-orbit splitting in doped nanocrystalline silicon: k·p calculations," *Physical Review B*, vol. 76, no. 4, Article ID 045335, 12 pages, 2007.

[74] B. Delley and E. F. Steigmeier, "Size dependence of band gaps in silicon nanostructures," *Applied Physics Letters*, vol. 67, no. 16, p. 2370, 1995.

[75] I. Vasiliev, S. Öğüt, and J. R. Chelikowsky, "*Ab initio* absorption spectra and optical gaps in nanocrystalline silicon," *Physical Review Letters*, vol. 86, no. 9, pp. 1813–1816, 2001.

[76] C. S. Garoufalis, A. D. Zdetsis, and S. Grimme, "High level *ab initio* calculations of the optical gap of small silicon quantum dots," *Physical Review Letters*, vol. 87, no. 27, Article ID 276402, 4 pages, 2001.

[77] H.-Ch. Weissker, J. Furthmüller, and F. Bechstedt, "Optical properties of Ge and Si nanocrystallites from *ab initio* calculations. II. Hydrogenated nanocrystallites," *Physical Review B*, vol. 65, no. 15, Article ID 155328, 7 pages, 2002.

[78] X.-H. Peng, S. Ganti, A. Alizadeh, P. Sharma, S. K. Kumar, and S. K. Nayak, "Strain-engineered photoluminescence of silicon nanoclusters," *Physical Review B*, vol. 74, no. 3, Article ID 035339, 5 pages, 2006.

[79] L.-W. Wang and A. Zunger, "Solving Schrödinger's equation around a desired energy: application to silicon quantum dots," *The Journal of Chemical Physics*, vol. 100, no. 3, pp. 2394–2397, 1994.

[80] S. Öğüt, J. R. Chelikowsky, and S. G. Louie, "Quantum confinement and optical gaps in Si nanocrystals," *Physical Review Letters*, vol. 79, no. 9, pp. 1770–1773, 1997.

[81] A. Franceschetti and A. Zunger, "Pseudopotential calculations of electron and hole addition spectra of InAs, InP, and Si quantum dots," *Physical Review B*, vol. 62, no. 4, pp. 2614–2623, 2000.

[82] C. Bulutay, "Interband, intraband, and excited-state direct photon absorption of silicon and germanium nanocrystals embedded in a wide band-gap lattice," *Physical Review B*, vol. 76, no. 20, Article ID 205321, 14 pages, 2007.

[83] S. Y. Ren and J. D. Dow, "Hydrogenated Si clusters: band formation with increasing size," *Physical Review B*, vol. 45, no. 12, pp. 6492–6496, 1992.

[84] N. A. Hill and K. B. Whaley, "Size dependence of excitons in silicon nanocrystals," *Physical Review Letters*, vol. 75, no. 6, pp. 1130–1133, 1995.

[85] Y. M. Niquet, C. Delerue, G. Allan, and M. Lannoo, "Method for tight-binding parametrization: application to silicon nanostructures," *Physical Review B*, vol. 62, no. 8, pp. 5109–5116, 2000.

[86] S. Lee, L. Jönsson, J. W. Wilkins, G. W. Bryant, and G. Klimeck, "Electron-hole correlations in semiconductor quantum dots with tight-binding wave functions," *Physical Review B*, vol. 63, no. 19, Article ID 195318, 13 pages, 2001.

[87] M. Rohlfing and S. G. Louie, "Excitonic effects and the optical absorption spectrum of hydrogenated Si clusters," *Physical Review Letters*, vol. 80, no. 15, pp. 3320–3323, 1998.

[88] C. Delerue, M. Lannoo, and G. Allan, "Excitonic and quasiparticle gaps in Si nanocrystals," *Physical Review Letters*, vol. 84, no. 11, pp. 2457–2460, 2000.

[89] E. Luppi, F. Iori, R. Magri, et al., "Excitons in silicon nanocrystallites: the nature of luminescence," *Physical Review B*, vol. 75, no. 3, Article ID 033303, 4 pages, 2007.

[90] T. Takagahara and K. Takeda, "Theory of the quantum confinement effect on excitons in quantum dots of indirect-gap materials," *Physical Review B*, vol. 46, no. 23, pp. 15578–15581, 1992.

[91] J. M. Ferreyra and C. R. Proetto, "Quantum size effects on excitonic Coulomb and exchange energies in finite-barrier semiconductor quantum dots," *Physical Review B*, vol. 60, no. 15, pp. 10672–10675, 1999.

[92] V. A. Burdov, "Electron and hole spectra of silicon quantum dots," *Journal of Experimental and Theoretical Physics*, vol. 94, no. 2, pp. 411–418, 2002.

[93] V. A. Burdov, "Dependence of the optical gap of Si quantum dots on the dot size," *Semiconductors*, vol. 36, no. 10, pp. 1154–1158, 2002.

[94] A. S. Moskalenko and I. N. Yassievich, "Excitons in Si nanocrystals," *Physics of the Solid State*, vol. 46, no. 8, pp. 1508–1519, 2004.

[95] A. S. Moskalenko, J. Berakdar, A. A. Prokofiev, and I. N. Yassievich, "Single-particle states in spherical Si/SiO_2 quantum dots," *Physical Review B*, vol. 76, no. 8, Article ID 085427, 9 pages, 2007.

[96] M. Bruno, M. Palummo, A. Marini, R. Del Sole, and S. Ossicini, "From Si nanowires to porous silicon: the role of excitonic effects," *Physical Review Letters*, vol. 98, no. 3, Article ID 036807, 4 pages, 2007.

[97] L. Yang, C. D. Spataru, S. G. Louie, and M. Y. Chou, "Enhanced electron-hole interaction and optical absorption in a silicon nanowire," *Physical Review B*, vol. 75, no. 20, Article ID 201304, 4 pages, 2007.

[98] M. Voos, Ph. Uzan, C. Delalande, G. Bastard, and A. Halimaoui, "Visible photoluminescence from porous silicon: a quantum confinement effect mainly due to holes," *Applied Physics Letters*, vol. 61, no. 10, pp. 1213–1215, 1992.

[99] A. A. Kopylov, ""Two-hump" structure and parameters of the X minimum of the conduction band of cubic III-V semiconductors," *Soviet Physics. Semiconductors-USSR*, vol. 16, no. 12, pp. 1380–1383, 1982.

[100] C. Delerue and M. Lannoo, *Nanostructures: Theory and Modeling*, Springer, Berlin, Germany, 2004.

[101] N. M. Johnson, D. K. Biegelsen, M. D. Moyer, S. T. Chang, E. H. Poindexter, and P. J. Caplan, "Characteristic electronic defects at the $Si\text{-}SiO_2$ interface," *Applied Physics Letters*, vol. 43, no. 6, pp. 563–565, 1983.

[102] M. Nishida, "Electronic structure of silicon quantum dots: calculations of energy-gap redshifts due to oxidation," *Journal of Applied Physics*, vol. 98, no. 2, Article ID 023705, 6 pages, 2005.

[103] M. Luppi and S. Ossicini, "*Ab initio* study on oxidized silicon clusters and silicon nanocrystals embedded in SiO_2: beyond the quantum confinement effect," *Physical Review B*, vol. 71, no. 3, Article ID 035340, 15 pages, 2005.

[104] L. E. Ramos, J. Furthmüller, and F. Bechstedt, "Reduced influence of defects on oxidized Si nanocrystallites," *Physical Review B*, vol. 71, no. 3, Article ID 035328, 7 pages, 2005.

[105] D. Vuillaume, D. Deresmes, and D. Stiévenard, "Temperature-dependent study of spin-dependent recombination at silicon dangling bonds," *Applied Physics Letters*, vol. 64, no. 13, pp. 1690–1692, 1994.

[106] M. Lannoo, C. Delerue, and G. Allan, "Nonradiative recombination on dangling bonds in silicon crystallites," *Journal of Luminescence*, vol. 57, no. 1–6, pp. 243–247, 1993.

[107] D. Goguenheim and M. Lannoo, "Theoretical calculation of the electron-capture cross section due to a dangling bond at the Si(111)-SiO_2 interface," *Physical Review B*, vol. 44, no. 4, pp. 1724–1733, 1991.

[108] W. Kohn and J. M. Luttinger, "Theory of donor levels in silicon," *Physical Review*, vol. 97, no. 6, p. 1721, 1955.

[109] W. Kohn and J. M. Luttinger, "Theory of donor states in silicon," *Physical Review*, vol. 98, no. 4, pp. 915–922, 1955.

[110] A. Baldereschi, "Valley-orbit interaction in semiconductors," *Physical Review B*, vol. 1, no. 12, pp. 4673–4677, 1970.

[111] S. T. Pantelides and C. T. Sah, "Theory of localized states in semiconductors. I. New results using an old method," *Physical Review B*, vol. 10, no. 2, pp. 621–637, 1974.

[112] R. A. Faulkner, "Higher donor excited states for prolate-spheroid conduction bands: a reevaluation of silicon and germanium," *Physical Review*, vol. 184, no. 3, pp. 713–721, 1969.

[113] Z. Zhou, M. L. Steigerwald, R. A. Friesner, L. Brus, and M. S. Hybertsen, "Structural and chemical trends in doped silicon nanocrystals: first-principles calculations," *Physical Review B*, vol. 71, no. 24, Article ID 245308, 8 pages, 2005.

[114] S. Ossicini, E. Degoli, F. Iori, et al., "Simultaneously B- and P-doped silicon nanoclusters: formation energies and electronic properties," *Applied Physics Letters*, vol. 87, no. 17, Article ID 173120, 3 pages, 2005.

[115] L. E. Ramos, E. Degoli, G. Cantele, et al., "Structural features and electronic properties of group-III-, group-IV-, and group-V-doped Si nanocrystallites," *Journal of Physics: Condensed Matter*, vol. 19, no. 46, Article ID 466211, 12 pages, 2007.

[116] F. Iori, E. Degoli, R. Magri, et al., "Engineering silicon nanocrystals: theoretical study of the effect of codoping with boron and phosphorus," *Physical Review B*, vol. 76, no. 8, Article ID 085302, 14 pages, 2007.

[117] Q. Xu, J.-W. Luo, S.-S. Li, J.-B. Xia, J. Li, and S.-H. Wei, "Chemical trends of defect formation in Si quantum dots: the case of group-III and group-V dopants," *Physical Review B*, vol. 75, no. 23, Article ID 235304, 6 pages, 2007.

[118] V. A. Belyakov and V. A. Burdov, "Chemical-shift enhancement for strongly confined electrons in silicon nanocrystals," *Physics Letters A*, vol. 367, no. 1-2, pp. 128–134, 2007.

[119] V. A. Belyakov and V. A. Burdov, "Anomalous splitting of the hole states in silicon quantum dots with shallow acceptors," *Journal of Physics: Condensed Matter*, vol. 20, no. 2, Article ID 025213, 13 pages, 2008.

[120] S. Y. Ren, "Quantum confinement of edge states in Si crystallites," *Physical Review B*, vol. 55, no. 7, pp. 4665–4669, 1997.

[121] B. Delley and E. F. Steigmeier, "Quantum confinement in Si nanocrystals," *Physical Review B*, vol. 47, no. 3, pp. 1397–1400, 1993.

[122] T. Blomquist and G. Kirczenow, "Poisson-Schrödinger and *ab initio* modeling of doped Si nanocrystals: reversal of the charge transfer between host and dopant atoms," *Physical Review B*, vol. 71, no. 4, Article ID 045301, 9 pages, 2005.

[123] F. Trani, D. Ninno, G. Cantele, et al., "Screening in semiconductor nanocrystals: *ab initio* results and Thomas-Fermi theory," *Physical Review B*, vol. 73, no. 24, Article ID 245430, 9 pages, 2006.

[124] G. Cantele, E. Degoli, E. Luppi, et al., "First-principles study of *n*- and *p*-doped silicon nanoclusters," *Physical Review B*, vol. 72, no. 11, Article ID 113303, 4 pages, 2005.

[125] F. Iori, E. Degoli, E. Luppi, et al., "Doping in silicon nanocrystals: an *ab initio* study of the structural, electronic and optical properties," *Journal of Luminescence*, vol. 121, no. 2, pp. 335–339, 2006.

[126] Y. Hada and M. Eto, "Electronic states in silicon quantum dots: multivalley artificial atoms," *Physical Review B*, vol. 68, no. 15, Article ID 155322, 7 pages, 2003.

[127] D. V. Melnikov and J. R. Chelikowsky, "Quantum confinement in phosphorus-doped silicon nanocrystals," *Physical Review Letters*, vol. 92, no. 4, Article ID 046802, 4 pages, 2004.

[128] M. Lannoo, C. Delerue, and G. Allan, "Screening in semiconductor nanocrystallites and its consequences for porous silicon," *Physical Review Letters*, vol. 74, no. 17, pp. 3415–3418, 1995.

[129] S. Öğüt, R. Burdick, Y. Saad, and J. R. Chelikowsky, "*Ab initio* calculations for large dielectric matrices of confined systems," *Physical Review Letters*, vol. 90, no. 12, Article ID 127401, 4 pages, 2003.

[130] C. Delerue, M. Lannoo, and G. Allan, "Concept of dielectric constant for nanosized systems," *Physical Review B*, vol. 68, no. 11, Article ID 115411, 4 pages, 2003.

[131] X. Cartoixà and L.-W. Wang, "Microscopic dielectric response functions in semiconductor quantum dots," *Physical Review Letters*, vol. 94, no. 23, Article ID 236804, 4 pages, 2005.

[132] F. Trani, D. Ninno, and G. Iadonisi, "Tight-binding formulation of the dielectric response in semiconductor nanocrystals," *Physical Review B*, vol. 76, no. 8, Article ID 085326, 9 pages, 2007.

[133] A. Franceschetti and M. C. Troparevsky, "Screening of point charges in Si quantum dots," *Physical Review B*, vol. 72, no. 16, Article ID 165311, 4 pages, 2005.

[134] G. Onida, L. Reining, and A. Rubio, "Electronic excitations: density-functional versus many-body Green's-function approaches," *Reviews of Modern Physics*, vol. 74, no. 2, pp. 601–659, 2002.

[135] M. Shishkin, M. Marsman, and G. Kresse, "Accurate quasiparticle spectra from self-consistent *GW* calculations with vertex corrections," *Physical Review Letters*, vol. 99, no. 24, Article ID 246403, 4 pages, 2007.

[136] L.-W. Wang and X. Cartoixà, "Motif-based polarization model: calculations of the dielectric function and polarization in large nanostructures," *Physical Review B*, vol. 75, no. 20, Article ID 205334, 5 pages, 2007.

[137] L.-W. Wang and A. Zunger, "Dielectric constants of silicon quantum dots," *Physical Review Letters*, vol. 73, no. 7, pp. 1039–1042, 1994.

[138] R. Tsu and D. Babić, "Doping of a quantum dot," *Applied Physics Letters*, vol. 64, no. 14, pp. 1806–1808, 1994.

[139] R. Tsu, D. Babić, and L. Ioriatti Jr., "Simple model for the dielectric constant of nanoscale silicon particle," *Journal of Applied Physics*, vol. 82, no. 3, pp. 1327–1329, 1997.

[140] V. A. Belyakov and V. A. Burdov, "Fine splitting of electron states in silicon nanocrystal with a hydrogen-like shallow donor," *Nanoscale Research Letters*, vol. 2, no. 11, pp. 569–575, 2007.

[141] N. O. Lipari and A. Baldereschi, "Interpretation of acceptor spectra in semiconductors," *Solid State Communications*, vol. 25, no. 9, pp. 665–668, 1978.

[142] A. Baldereschi and N. O. Lipari, "Spherical model of shallow acceptor states in semiconductors," *Physical Review B*, vol. 8, no. 6, pp. 2697–2709, 1973.

[143] A. Baldereschi and N. O. Lipari, "Cubic contributions to the spherical model of shallow acceptor states," *Physical Review B*, vol. 9, no. 4, pp. 1525–1539, 1974.

[144] N. O. Lipari, A. Baldereschi, and M. L. W. Thewalt, "Central cell effects on acceptor spectra in Si and Ge," *Solid State Communications*, vol. 33, no. 3, pp. 277–279, 1980.

[145] A. Thränhardt, C. Ell, G. Khitrova, and H. M. Gibbs, "Relation between dipole moment and radiative lifetime in interface fluctuation quantum dots," *Physical Review B*, vol. 65, no. 3, Article ID 035327, 6 pages, 2002.

[146] D. I. Tetelbaum, V. A. Burdov, A. N. Mikhaylov, and S. A. Trushin, "About the phosphorus sensitization of silicon quantum dots in SiO_2 photoluminescence," in *10th International Symposium on Nanostructures: Physics and Technology*, vol. 5023 of *Proceedings of SPIE*, pp. 186–189, St. Petersburg, Russia, June 2003.

[147] M. S. Hybertsen, "Absorption and emission of light in nanoscale silicon structures," *Physical Review Letters*, vol. 72, no. 10, pp. 1514–1517, 1994.

[148] C. Delerue, G. Allan, and M. Lannoo, "Electron-phonon coupling and optical transitions for indirect-gap semiconductor nanocrystals," *Physical Review B*, vol. 64, no. 19, Article ID 193402, 4 pages, 2001.

[149] V. A. Belyakov, V. A. Burdov, D. M. Gaponova, A. N. Mikhaylov, D. I. Tetelbaum, and S. A. Trushin, "Phonon-assisted radiative electron-hole recombination in silicon quantum dots," *Physics of the Solid State*, vol. 46, no. 1, pp. 27–31, 2004.

[150] O. J. Glembocki and F. H. Pollak, "Calculation of the γ-δ electron-phonon and hole-phonon scattering matrix elements in silicon," *Physical Review Letters*, vol. 48, no. 6, pp. 413–416, 1982.

[151] O. J. Glembocki and F. H. Pollak, "Relative intensities of indirect transitions: electron-phonon and hole-phonon interaction matrix elements in Si (TO) and GaP (LA,TA)," *Physical Review B*, vol. 25, no. 2, pp. 1193–1204, 1982.

[152] I. Mihalcescu, J. C. Vial, A. Bsiesy, et al., "Saturation and voltage quenching of porous-silicon luminescence and the importance of the Auger effect," *Physical Review B*, vol. 51, no. 24, pp. 17605–17613, 1995.

[153] A. A. Prokofiev, A. S. Moskalenko, and I. N. Yassievich, "Theoretical modeling of excitation and de-excitation processes of Er in SiO_2 with Si nanocrystals," *Journal of Luminescence*, vol. 121, no. 2, pp. 222–225, 2006.

[154] D. V. Talapin, A. L. Rogach, A. Kornowski, M. Haase, and H. Weller, "Highly luminescent monodisperse CdSe and CdSe/ZnS nanocrystals synthesized in a hexadecylamine-trioctylphosphine oxide-trioctylphospine mixture," *Nano Letters*, vol. 1, no. 4, pp. 207–211, 2001.

[155] R. Espiau de Lamaëstre and H. Bernas, "Significance of lognormal nanocrystal size distributions," *Physical Review B*, vol. 73, no. 12, Article ID 125317, 9 pages, 2006.

[156] R. Espiau de Lamaëstre and H. Bernas, "Ion beam-induced quantum dot synthesis in glass," *Nuclear Instruments and Methods in Physics Research, Section B*, vol. 257, no. 1-2, pp. 1–5, 2007.

[157] R. B. Bergmann, J. Köhler, R. Dassow, C. Zaczek, and J. H. Werner, "Nucleation and growth of crystalline silicon films on glass for solar cells," *Physica Status Solidi (A)*, vol. 166, no. 2, pp. 587–602, 1998.

[158] R. B. Bergmann, J. Krinke, H. P. Strunk, and J. H. Werner, "Deposition and characterization of polycrystalline silicon films on glass for thin film solar cells," in *Materials Research Society Symposium Proceedings*, vol. 467, pp. 325–330, San Francisco, Calif, USA, March 1997.

[159] S. K. Kurtz and F. M. A. Carpay, "Microstructure and normal grain growth in metals and ceramics—I: theory," *Journal of Applied Physics*, vol. 51, no. 11, pp. 5725–5744, 1980.

[160] R. Lockwood, A. Hryciw, and A. Meldrum, "Nonresonant carrier tunneling in arrays of silicon nanocrystals," *Applied Physics Letters*, vol. 89, no. 26, Article ID 263112, 3 pages, 2006.

[161] V. Vinciguerra, G. Franzò, F. Priolo, F. Iacona, and C. Spinella, "Quantum confinement and recombination dynamics in silicon nanocrystals embedded in Si/SiO_2 superlattices," *Journal of Applied Physics*, vol. 87, no. 11, pp. 8165–8173, 2000.

[162] M. Glover and A. Meldrum, "Effect of "buffer layers" on the optical properties of silicon nanocrystal superlattices," *Optical Materials*, vol. 27, no. 5, pp. 977–982, 2005.

[163] A. Meldrum, L. A. Boatner, C. W. White, and R. C. Ewing, "Ion irradiation effects in nonmetals: formation of nanocrystals and novel microstructures," *Materials Research Innovations*, vol. 3, no. 4, pp. 190–204, 2000.

[164] F. Huisken, G. Ledoux, O. Guillois, and C. Reynaud, "Light-emitting silicon nanocrystals from laser pyrolysis," *Advanced Materials*, vol. 14, no. 24, pp. 1861–1865, 2002.

[165] M. Cazzanelli, D. Navarro-Urriós, F. Riboli, et al., "Optical gain in monodispersed silicon nanocrystals," *Journal of Applied Physics*, vol. 96, no. 6, pp. 3164–3171, 2004.

[166] I. Y. Choi, K. H. Byoun, M. H. Jung, H.-J. Lim, and H. W. Lee, "Synthesis of cyano cyclic olefins through ring-closing metathesis," *Bulletin of the Korean Chemical Society*, vol. 25, no. 9, pp. 1305–1306, 2004.

[167] L. Pavesi and M. Ceschini, "Stretched-exponential decay of the luminescence in porous silicon," *Physical Review B*, vol. 48, no. 23, pp. 17625–17628, 1993.

[168] H. E. Roman and L. Pavesi, "Monte Carlo simulations of the recombination dynamics in porous silicon," *Journal of Physics: Condensed Matter*, vol. 8, no. 28, pp. 5161–5187, 1996.

[169] O. Guillois, N. Herlin-Boime, C. Reynaud, G. Ledoux, and F. Huisken, "Photoluminescence decay dynamics of noninteracting silicon nanocrystals," *Journal of Applied Physics*, vol. 95, no. 7, pp. 3677–3682, 2004.

[170] M. N. Berberan-Santos, E. N. Bodunov, and B. Valeur, "Mathematical functions for the analysis of luminescence decays with underlying distributions 1. Kohlrausch decay function (stretched exponential)," *Chemical Physics*, vol. 315, no. 1-2, pp. 171–182, 2005.

[171] J. Heitmann, F. Müller, M. Zacharias, and U. Gösele, "Silicon nanocrystals: size matters," *Advanced Materials*, vol. 17, no. 7, pp. 795–803, 2005.

[172] S. Tiwari, F. Rana, H. Hanafi, A. Hartstein, E. F. Crabbé, and K. Chan, "A silicon nanocrystals based memory," *Applied Physics Letters*, vol. 68, no. 10, pp. 1377–1379, 1996.

[173] T. Z. Lu, M. Alexe, R. Scholz, V. Talelaev, and M. Zacharias, "Multilevel charge storage in silicon nanocrystal multilayers," *Applied Physics Letters*, vol. 78, no. 20, Article ID 202110, 3 pages, 2005.

[174] S. Muto, T. Inata, A. Tackeuchi, Y. Sugiyama, and T. Fujii, "Longitudinal-optical-phonon assisted tunneling in tunneling bi-quantum well structures," *Applied Physics Letters*, vol. 58, no. 21, pp. 2393–2395, 1991.

[175] S. Haacke, N. T. Pelekanos, H. Mariette, M. Zigone, A. P. Heberle, and W. W. Rühle, "Tunneling dynamics in CdTe/(Cd,Zn)Te asymmetric double-quantum-well structures," *Physical Review B*, vol. 47, no. 24, pp. 16643–16646, 1993.

[176] A. Tackeuchi, T. Kuroda, K. Mase, Y. Nakata, and N. Yokoyama, "Dynamics of carrier tunneling between vertically aligned double quantum dots," *Physical Review B*, vol. 62, no. 3, pp. 1568–1571, 2000.

[177] T. Förster, "Zwischenmolekulare Energiewanderung und Fluoreszenz," *Annalen der Physik*, vol. 2, no. 1-2, pp. 55–75, 1948.

[178] C. B. Murray, C. R. Kagan, and M. G. Bawendi, "Synthesis and characterization of monodisperse nanocrystals and close-packed nanocrystal assemblies," *Annual Review of Materials Science*, vol. 30, pp. 545–610, 2000.

[179] G. Liu and B. Jacquier, Eds., *Spectroscopic Properties of Rare Earths in Optical Materials*, Springer, New York, NY, USA, 2005.

[180] T. Miyakawa and D. L. Dexter, "Phonon sidebands, multiphonon relaxation of excited states, and phonon-assisted energy transfer between ions in solids," *Physical Review B*, vol. 1, no. 7, pp. 2961–2969, 1970.

[181] R. Reisfeld, "Rare earths complexes in sol gel glasses," *Materials Science*, vol. 20, pp. 5–18, 2002.

[182] J. L. Kennedy and N. Djeu, "Energy transfer in rare earth doped $Y_3Al_5O_{12}$ at very high temperatures," *Journal of Luminescence*, vol. 101, no. 1-2, pp. 147–153, 2003.

[183] M. P. Hehlen, N. J. Cockroft, T. R. Gosnell, and A. J. Bruce, "Spectroscopic properties of Er^{3+}- and Yb^{3+}-doped soda-lime silicate and aluminosilicate glasses," *Physical Review B*, vol. 56, no. 15, pp. 9302–9318, 1997.

[184] F. Pellé, N. Gardant, and F. Auzel, "Effect of excited-state population density on nonradiative multiphonon relaxation rates of rare-earth ions," *Journal of the Optical Society of America B*, vol. 15, no. 2, pp. 667–679, 1998.

[185] N. Yamada, S. Shionoya, and T. Kushida, "Phonon-assisted energy transfer between trivalent rare earth ions," *Journal of the Physical Society of Japan*, vol. 32, no. 6, pp. 1577–1586, 1972.

[186] H. Kuhn, "Classical aspects of energy transfer in molecular systems," *The Journal of Chemical Physics*, vol. 53, no. 1, pp. 101–108, 1970.

[187] L. Dal Negro, M. Cazzanelli, B. Danese, et al., "Light amplification in silicon nanocrystals by pump and probe transmission measurements," *Journal of Applied Physics*, vol. 96, no. 10, pp. 5747–5755, 2004.

[188] K. Luterová, K. Dohnalová, F. Trojánek, et al., "Porous silicon grains in SiO_2 matrix: ultrafast photoluminescence and optical gain," *Journal of Non-Crystalline Solids*, vol. 352, no. 28-29, pp. 3041–3046, 2006.

[189] P. M. Fauchet, J. Ruan, H. Chen, et al., "Optical gain in different silicon nanocrystal systems," *Optical Materials*, vol. 27, no. 5, pp. 745–749, 2005.

[190] M. H. Nayfeh, N. Barry, J. Therrien, O. Akcakir, E. Gratton, and G. Belomoin, "Stimulated blue emission in reconstituted films of ultrasmall silicon nanoparticles," *Applied Physics Letters*, vol. 78, no. 8, pp. 1131–1133, 2001.

[191] J. Valenta, K. Luterová, R. Tomasiunas, K. Dohnalová, B. Hönerlage, and I. Pelant, "Optical gain measurements with variable stripe length technique," in *Towards the First Silicon Laser*, L. Pavesi, S. Gaponenko, and L. Dal Negro, Eds., vol. 93 of *NATO Science Series*, pp. 223–242, Kluwer Academic Publishers, Dordrecht, The Netherlands, 2003.

[192] H. Lee, J. H. Shin, and N. Park, "Performance analysis of nanocluster-Si sensitized Er-doped waveguide amplifier using top-pumped 470 nm LED," *Optics Express*, vol. 13, no. 24, pp. 9881–9889, 2005.

[193] V. I. Klimov, S. A. Ivanov, J. Nanda, et al., "Single-exciton optical gain in semiconductor nanocrystals," *Nature*, vol. 447, no. 7143, pp. 441–446, 2007.

[194] C. M. Hessel, M. A. Summers, A. Meldrum, M. Malac, and J. G. C. Veinot, "Direct patterning, conformal coating, and erbium doping of luminescent nc-Si/SiO_2 thin films from solution processable hydrogen silsesquioxane," *Advanced Materials*, vol. 19, no. 21, pp. 3513–3516, 2007.